# Anodic Oxidation Nanolithography on Graphene Flakes through an Atomic Force Microscope

# Anodische Oxidation Nanolitografie auf Graphene Schichten mittels Rasterkraftmikroskop

**Lorenzo Volta**

München 2024

# Anodic Oxidation Nanolithography on Graphene Flakes through an Atomic Force Microscope

**Lorenzo Volta**

Chair of Experimental Solid State Physics - Quantum Materials
Faculty of Physics
Ludwig–Maximilians–Universität München

submitted by
Lorenzo Volta

Supervisors:
Prof. Dr. Dimitri K. Efetov
Jaime Díez-Mérida,

Munich, 01.01.2024

# Acknowledgements

# Abstract

This thesis explores a technique called anodic oxidation nanolithography to create patterns on exfoliated graphene using a specialized microscope called an Atomic Force Microscope (AFM). The main goal is to demonstrate the feasibility of lifting off the patterned graphene, which could be useful for fabricating devices to study the properties of graphene. The aim is to provide a simple guide for anyone interested in utilizing this technique.

We will delve into the basic steps of anodic oxidation nanolithography, focusing on elements crucial for successfully achieving patterned graphene. The results of our experiments indicate that this method works well and could serve as a valuable tool for fabricating devices with graphene. Using this new approach facilitates fabrication since etching of the substrate is not mandatory. This thesis not only aids in comprehending the process but also aspires to be a straightforward guide for others interested in employing this method.

In summary, this thesis focuses on utilizing an Atomic Force Microscope to create patterns on graphene and is designed to be a helpful guide for anyone interested in undertaking the same.

# Contents

# Chapter 1

# Introduction

In the last few decades, two-dimensional (2D) materials have become a significant focus of experimental solid-state physics, particularly emphasizing two-dimensional sheets. In the 20th century, the existence of these materials was highly debated, as classical physics concepts contradicted them. Consequently, a more quantum-based approach was adopted to describe the electronic properties of these materials. This shift led to extensive research and the production of novel materials. One commonly utilized method for determining material characteristics is the Atomic Force Microscope (AFM). The interaction of the machine with atomic forces enables the creation of topographical imaging, but the impact of an AFM extends beyond this. As demonstrated, we can leverage chemical reactions to shape materials. This technique, combined with the stacking of other 2D materials, is poised to enable the development of high-quality graphene samples, such as electrostatically gate-defined Hall bars or superconducting interference devices.

In Chapter 2, we delve into the essential theoretical background. Beginning with graphene as an atomically thin layer, we then establish connections to multi-layered graphene. Subsequently, we discuss achieving the visibility of graphene under a light microscope. To conclude this chapter, we transition to the AFM, detailing its operating methods, with special focus on anodic oxidation in scanning probe microscopy (SPM).

Chapter 3 comprehensively explains all the experimental procedures employed. This encompasses processes ranging from chip preparation and exfoliation to the final pick-up of cut graphite. The anodic oxidation process, along with the experimented patterns, is particularly detailed, including AFM parameters and design creation.

Chapter 4 involves presenting the results obtained through the described methods, as well as discussing them. We start with humidity as a relevant parameter and progress to the patterns, emphasizing the development of a ring structure and the preservation of graphite squares.

The entirety of the findings are summarized in the last chapter 5, where future directions of work are also contemplated.

# Chapter 2

# Fundementals

## 2.1  Single Layer Graphene

In graphene, each atom in a sheet is connected with the three nearest neighbouring atoms through covalent bonds. The structural flexibility of graphene is shown in the electronic properties. When a carbon atom forms a double bond, it undergoes $sp^2$ hybridization, combining one s and two p orbitals to create three $sp^2$ hybrid orbitals in a trigonal planar arrangement. The remaining unhybridized $p$ orbital forms a $\pi$ bond through sidewise overlap with a corresponding p orbital from another atom, contributing to the stability of molecules with double bonds. The neighbouring carbon atoms (one blue and one yellow) of one sheet are held together by $\sigma$ bonds, creating the robustness of the structure. Therefore, the hexagonal honeycomb is formed from two lattices bonding together.[2, 3].

$$\vec{a_1} = \frac{a}{2} \cdot (3, \sqrt{3}), \tag{2.1}$$

$$\vec{a_2} = \frac{a}{2} \cdot (3, -\sqrt{3}), \tag{2.2}$$

$$\vec{\delta_1} = \frac{a}{2}(1, \sqrt{3}) \tag{2.3}$$

$$\vec{\delta_2} = \frac{a}{2}(1, -\sqrt{3}) \tag{2.4}$$

$$\vec{\delta_3} = -a(1, 0) \tag{2.5}$$
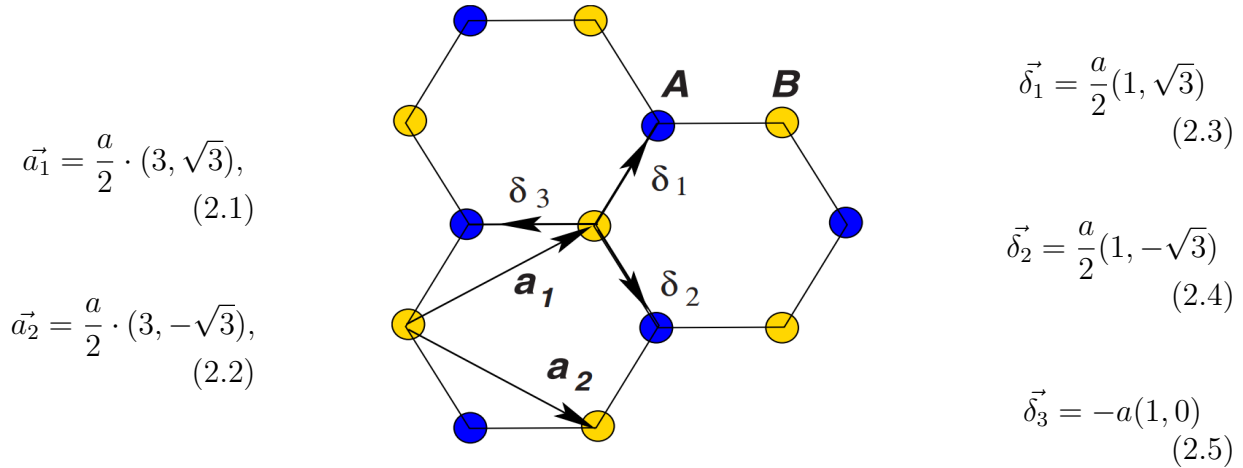
**Figure 2.1:** Lattice structure of graphene, made out of two interpenetrating triangular lattices ($\vec{a_1}$ and $\vec{a_2}$ are the lattice unit vectors, and $\vec{\delta_i}$ ($i = 1, 2, 3$) are the nearest-neighbor vectors) [2].

The vectors written on the left and right of the image include the distance between two carbon atoms $a \approx 1.42$ Å. From this structure and image the Brillouin zone structure can be derived, including its vectors, which are given by:

$$\vec{b_1} = \frac{2\pi}{3a} \cdot (1, \sqrt{3}), \tag{2.6}$$

$$K = (\frac{2\pi}{3a}, \frac{2\pi}{3\sqrt{3}a}) \tag{2.8}$$

$$\vec{b_2} = \frac{2\pi}{3a} \cdot (1, -\sqrt{3}), \tag{2.7}$$

$$K' = (\frac{2\pi}{3a}, -\frac{2\pi}{3\sqrt{3}a}) \tag{2.9}$$
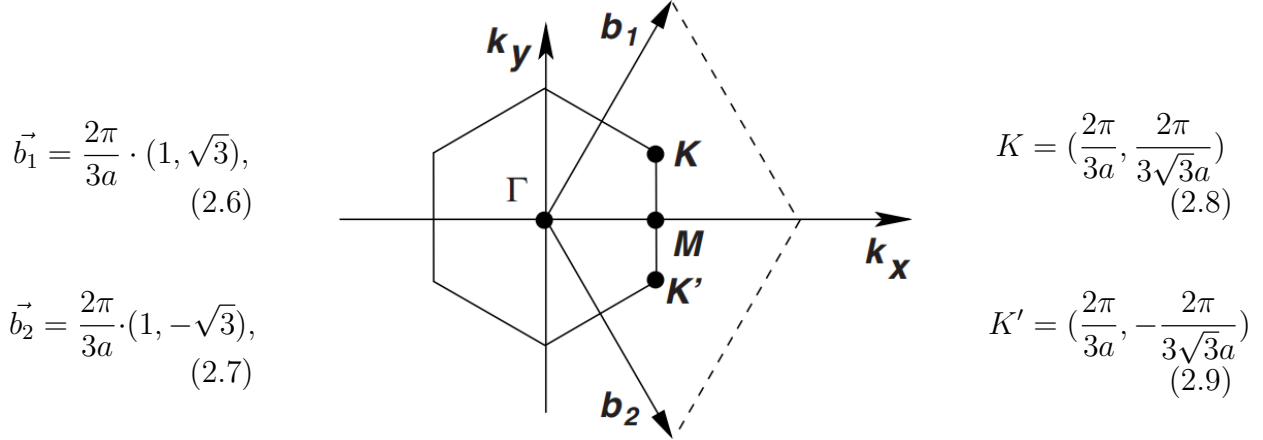


**Figure 2.2:** Corresponding Brillouin zone derived from Fig.2.1, including the Dirac cones located at the points K and K´.
Adapted from [2]

In order to describe the electronic transport properties, we usually would use the Schrödinger equation [4], but in the case of graphene, it is easier to describe the carriers through the Hamiltonian. From above equations, one can construct the tight-binding Hamiltonian, whereas it needs to be taken into consideration, that the electrons can hop to both nearest- and next-nearest-neighbor atoms, and therefore has the form [2]:

$$H = -t \sum_{<i,j>\sigma} (a_{\sigma,i}^\dagger \cdot b_{\sigma,j} + H.c.) - t' \sum_{<<i,j>>\sigma} (a_{\sigma,i}^\dagger \cdot a_{\sigma,j} + b_{\sigma,i}^\dagger \cdot b_{\sigma,j} + H.c.), (\hbar = 1) \tag{2.10}$$

hereby, $a_{i,\sigma}$ creates an electron with spin $\sigma$ on site $R_i$ on sublattice A (an equivalent definition is used for sublattice B), $t$ ($\approx 2.8$ eV) is the nearest-neighbor hopping energy (hopping between different sublattices), and $t'$ is the next nearest-neighbor hopping energy (hopping in the same sublattice). From the Hamiltonian one can write the energy band as:

$$E_\pm = \pm t\sqrt{3 + f(k)} - t' f(k), \tag{2.11}$$

$$f(k) = 2 \cdot \cos(\sqrt{3}k_y a) + 4 \cdot \cos(\frac{\sqrt{3}}{2}k_y a) \cdot \cos(\frac{3}{2}k_x a), \tag{2.12}$$

where the plus sign stands for the upper band and the minus sign stands for the lower band. The band structure for small $q$ relative to the Dirac points K or K' is given by:

$$E_\pm(q) \approx \pm \hbar v_F + \mathcal{O}((\frac{q}{k})^2), \tag{2.13}$$

with $q$ being the dispersion momentum, connected as $k = K + q$

The calculated band structure (shown in Fig. 2.3), as-well-as above equations, show that the spectrum is symmetric around $E_k = 0$ if $t' = 0$. Otherwise, for values of $t' \neq 0$ the symmetry of the electron-hole bands is broken. The zoom-in shows the band structure close to one of the Dirac points (at the $K$ and $K'$ points in the Brillouin zone). The Dirac cones show that graphene is a zero-gap semi-metal.

$$K = (\frac{2\pi}{3a}, \frac{2\pi}{3\sqrt{3}a}) \qquad (2.14)$$

$$K' = (\frac{2\pi}{3a}, -\frac{2\pi}{3\sqrt{3}a}) \qquad (2.15)$$
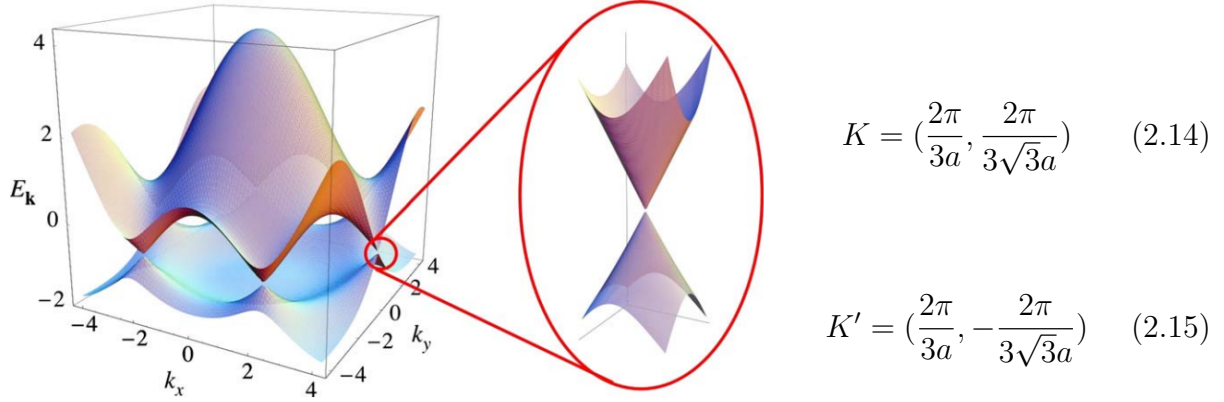
**Figure 2.3:** <u>Left:</u> Energy spectrum for finite values of $t$ and $t'$, with $t = 2.7$eV and $t' = -0.2t$. <u>Right:</u> Zoom in of the energy band close to one of the Dirac points. [2]

For low energy limits, where $E = h\nu$, the dispersion is linear and electrons in materials like graphene behave as massless Dirac fermions, characterizing graphene with fascinating electronic properties.

## 2.2   Bilayer Graphene

### 2.2.1   Van-der-Waals Interactions

Graphite is a 2D material made out of many graphene layers which are held together by van-der-Waals forces. These forces allow the material to be mechanically exfoliated. The mechanism of how Van-der-Waals forces hold the material together is as follows. Through the movements between the electrons around the atoms core, their symmetry is constantly disturbed and therefore a fluctuating electric dipole gets formed [5]. The dipole $p_a$ from the atom A induces a dipole in the neighboring atom B, creating a dipole $p_b$. The interaction between the two dipoles is attracting and the force in between the two dipoles is known as Van-der-Waals force. From the interaction between dipoles one can calculate the Lennard-Jones-Potential:

$$E_{LJ-pot}(r) = 4\epsilon \cdot \left[ \left( \frac{\sigma}{r} \right)^{12} - \left( \frac{\sigma}{r} \right)^{6} \right], \quad (2.16)$$

$$E_{pot}(r) = -\frac{C}{r^6} \qquad (2.17)$$
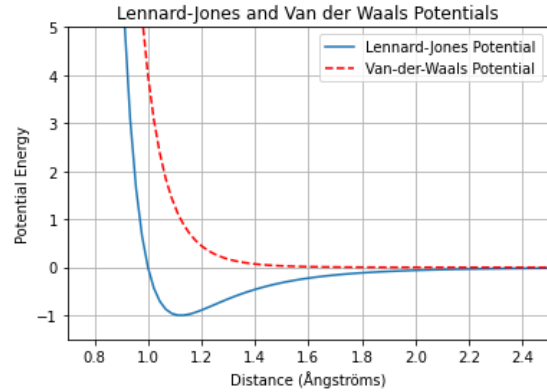


**Figure 2.4:** <u>Blue curve:</u> Lennard-Jones-Potential, <u>Red curve:</u> Van-der-Waals Potential (both for a two atom system). $\epsilon$ is the depth of the potential well, $\sigma$ is the distance at which the particle-particle energy $V$ is zero, $r$ is the particle-particle distance [5, 6].

The potential described from Eq. 2.17 is attractive, recognisable from the minus sign, and it is short ranged since it drops of $\propto 1/r^6$. Once the space between two atoms increases over minimum distance ($r \gtrsim 1.7$), other forces start to overcome the Van-der-Waals forces. The binding energy between two layers of graphene is just 0.07 eV.

## 2.2.2 Bilayer Graphene properties

The tight-binding model devised for graphene can be readily applied to stacks featuring a finite number of graphene layers, with the most straightforward adaptation seen in bilayer graphene.
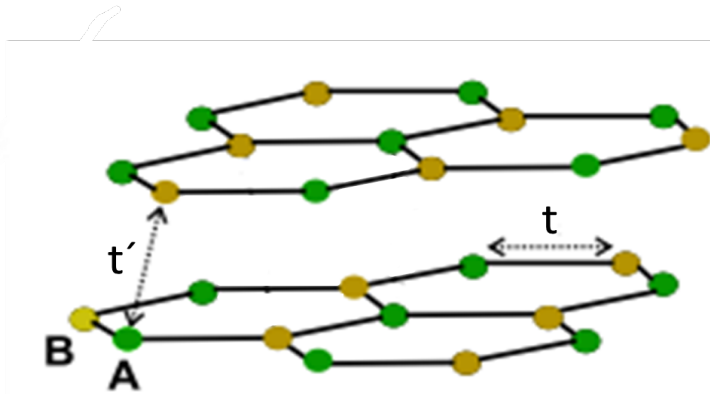


**Figure 2.5:** Lattice structure of the bilayer with the various hopping parameters. The A-sublattice are indicated by the green spheres, the B-sublattice by the gold ones. $t$ is the nearest neighbour and $t'$ is the next-nearest neighbour. [2]

The structure of graphite, with AB-stacking of graphene are visible in Fig. 2.5, including the constants $t$ and $t'$, labeling the corresponding pair of atoms associated. Solving the Hamiltonian gives two parabolic bands, $E_{k,\pm} \approx \pm v_F^2 k^2/t_\perp$, which touch at $E = 0$, like visible below in Fig. 2.6:
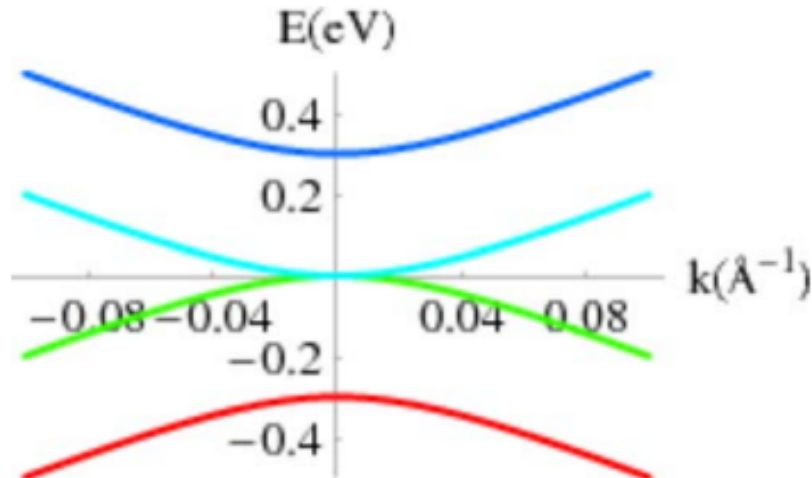


**Figure 2.6:** Band Structure for bilayer graphene for $V = 0$ and $t' = 0$.[2]

The spectrum is electron-hole symmetric, with two additional bands starting at $\pm t'$. Within this approximation, the bilayer is metallic, with a constant density of states, meaning that the number of electronic states per unit energy in a given system is consistent.

### 2.2.3    MATBG and Moiré patterns

As previously explained, graphene is a 2D material with the form of a honeycomb lattice and $sp^2$ bonds. When two layers are stacked on top of the other with lateral displacement bilayer graphene is formed. Due to the delocalization of atoms in the upper layer as opposed to the more localized nature of atoms in the lower layer, certain defects may manifest in twisted bilayer graphene. This distinction in atomic behavior between the top and bottom layers contributes to the emergence of structural irregularities or imperfections within the material. These defects can also take place through rotation of the upper layer in respect to the bottom one, forming a large-scale interference pattern known as Moiré pattern [7, 8].
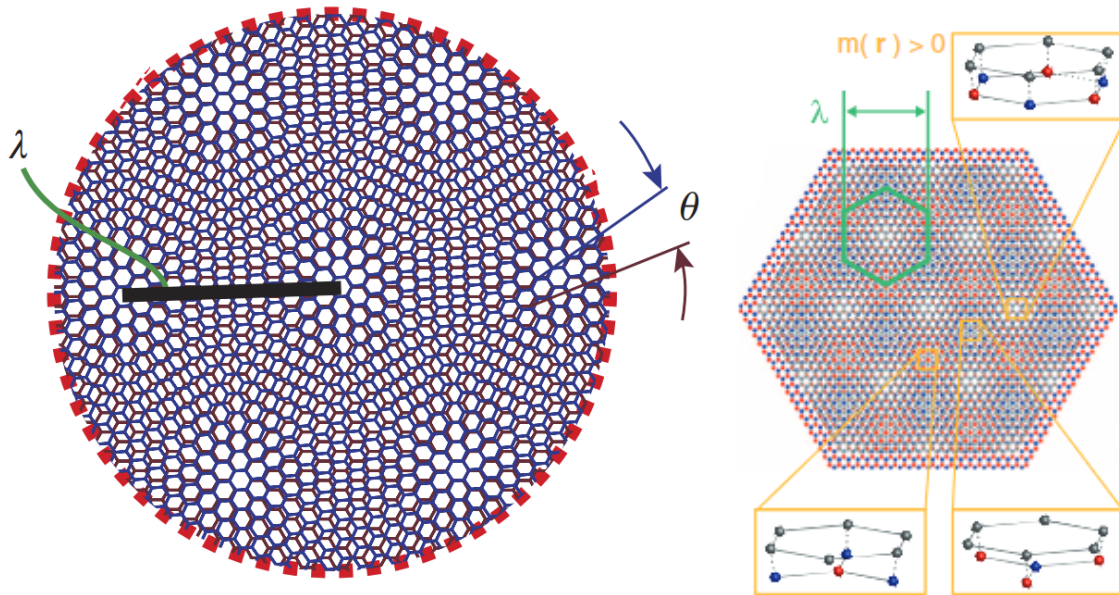


**Figure 2.7:** <u>Left:</u> Schematic for twisted bilayer graphene at an angle $\theta$ [9]: <u>Right:</u> Schematic of Moiré pattern for graphene (grey) and hBN (red and blue), for $\theta = 0$. The Moiré unit cell is outlined in green[10].

First calculations in 2011 showed a series of discrete minima at certain twist angles, for which the bands were flattened. For specific twist angles, approximately 1.1° for the first magic-angle, the interlayer hybridization induces nearly flat low-energy bands near zero Fermi energy. The difference between the two wavevectors $K$ (or $K'$) gives rise to a mini Brillouin zone. The Dirac cones near either of these points mix through interlayer hybridization, leading to energy gaps opening near the intersection of the Dirac cones (see Fig. 2.8 and the renormalization of the Fermi velocity at the Dirac points. Qualitatively, the flattening of energy bands near the magic angle arises from the interplay between kinetic energy and interlayer hybridization energy.
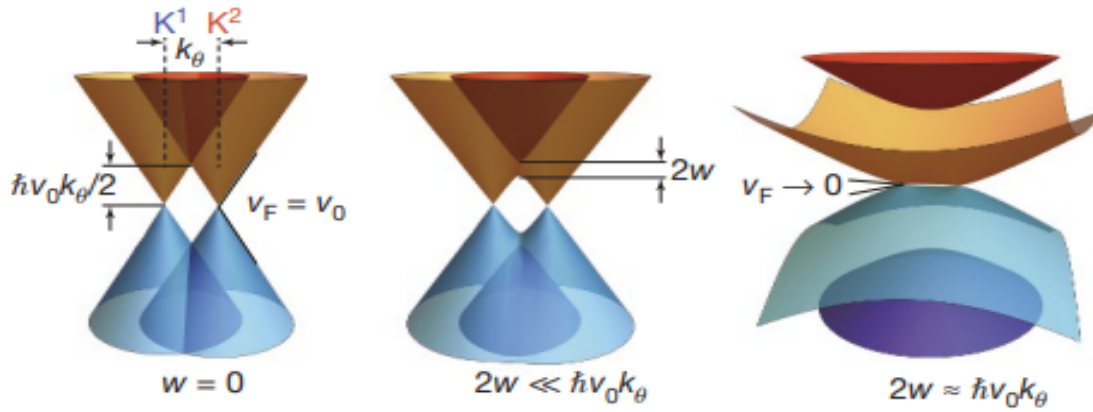
**Figure 2.8:** Illustration of the effect of interlayer hybridization for three different hybridization energies. Adapted from Fig.1 of [9]

At the theoretically calculated magic angles $\theta_{magic}^{(i)}$, with $i = 1, 2, ...$, the Fermi velocity becomes zero. Since the difference of the mismatched lattice leads to the formation of a Moiré Pattern with wavelength $\lambda_M(\theta)$, that can be much larger than the lattice constant, the effect of Moiré has a big influence on the electronic structure of graphene. It will give rise to a super-potential, creating a new artificial 2D lattice, which will correspond to the overall periodicity of the stacked layers and so for forming a superlattice. The smaller the mismatch between the layers, the larger the superlattice unit cell, leading to a smaller mini-Brillouin zone [9, 11].
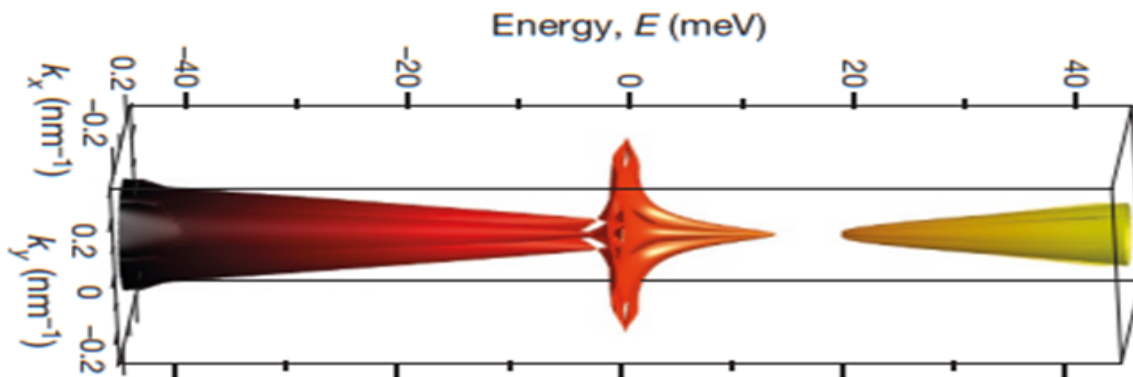


**Figure 2.9:** The band energy E of Twisted Bilayer Graphene at $\theta = 1.05°$ in the first mini Brillouin zone of the superlattice.
Adapted from Fig. 1 of [11]

## 2.3 Contrast of graphene under a microscope

In order to distinguish graphene monolayers, one could use Raman spectroscopy, though having the issue that it does not easily and quickly allow the search for graphene layers [12]. Therefore, we use an optical microscope, because once graphene is deposited on an oxidized $Si/SiO_2$-substrate, these thin flakes are sufficient to cause a change in the optical path, without blocking the light off completely. This allows us to see a contrast in the colours which the human eye shows, so that we can differentiate between different graphene flakes on a small area.
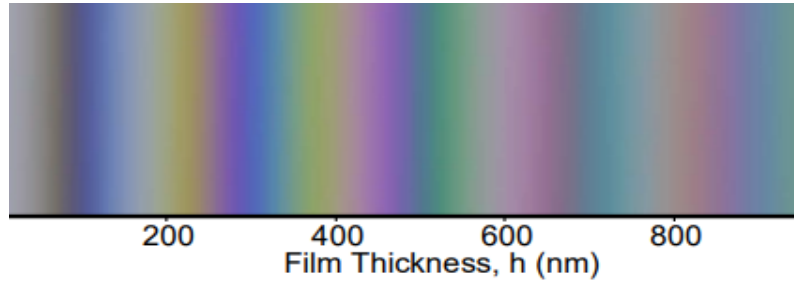


**Figure 2.10:** Apparent colour of a $SiO_2$ film on a silicon substrate as a function of thickness with a source and viewing angle of $\theta = 0°$ [13].

The dependency of contrast is explained by using a model based on Fresnel's Law [14], allowing to understand the differences caused from the thickness of $SiO_2$ and the wavelength $\lambda$. The silicium layer is characterized by a complex refractive index $n_3(\lambda)$, where it is directly proportional to $\lambda$. Moreover, the thickness of the oxidized part ($SiO_2$), is also dependent on a refractive index $n_2(\lambda)$, but only with a real part. The two indices together describe the whole range of interference colors for oxidized Si wafers [13]. Lastly, single-layer graphene is assumed to have a thickness of $d_1 = 0.34$ nm, equal to the extension of the $\pi$ orbitals out-of-plane and a complex refractive index $n_1(\lambda)$, while the refractive index can also be described through the one of bulk graphite, therefore $n_1(\lambda) \approx 2.6 - 1.3i$. By considering the geometry, we can show how the intensity of the reflected light is written:[14, 15]

$$I(n_1) = | \left( r_1 \cdot e^{i(\phi_1+\phi_2)} + r_2 \cdot e^{-i(\phi_1-\phi_2)} + r_3 \cdot e^{-i(\phi_1+\phi_2)} + r_1 \cdot r_2 \cdot r_3 \cdot e^{i(\phi_1+\phi_2)} \right.$$
$$\left. \times [e^{i(\phi_1+\phi_2)} + r_1 \cdot r_2 \cdot e^{-i(\phi_1-\phi_2)} + r_1 \cdot r_3 \cdot e^{-i(\phi_1+\phi_2)} + r_2 \cdot r_3 \cdot e^{i(\phi_1-\phi_2)}]^{-1} |^2 \tag{2.18}$$

$$r_1 = \frac{n_0 - n_1}{n_0 + n_1}, \quad (2.19) \qquad r_2 = \frac{n_1 - n_2}{n_1 + n_2}, \quad (2.20) \qquad r_3 = \frac{n_2 - n_3}{n_2 + n_3}, \quad (2.21)$$

are the relative indices of refraction. The changes in the optical path lead to phase shifts, expressed as $\phi_1 = \frac{2\pi n_1 d_1}{\lambda}$ and $\phi_2 = \frac{2\pi n_2 d_2}{\lambda}$.

Like this, it is possible to calculate the contrast $C$, which is defined as the relative intensity of reflected light in the presence $(n_1 \neq 1)$ and absence $(n_1 = n_0 = 1)$ of graphene:

$$C = \frac{I(n_1 = 1) - I(n_1)}{I(n_1 = 1)}. \tag{2.22}$$

Eq. 2.22 allows then to plot the contrast as a function of wavelenght and $SiO_2$ thickness. On the right side, the expected contrast is shown.

There have been different approaches in the thickness of $SiO_2$, as well as in the quality of the camera, as they change the result drastically, but conclusions led to 300 nm being the best thickness. For example, a 5% change in the thickness of $SiO_2$ (315 nm instead of 300 nm), significantly lowers the contrast. The origin of the optical contrast seen through a
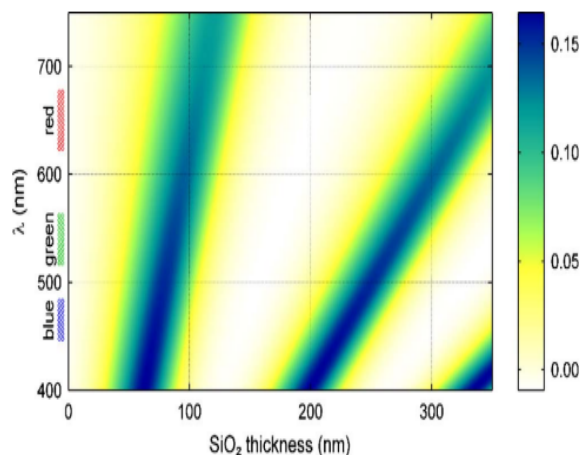


**Figure 2.11:** Color plot of the contrast dependent to wavelenght and $SiO_2$ thickness [14].
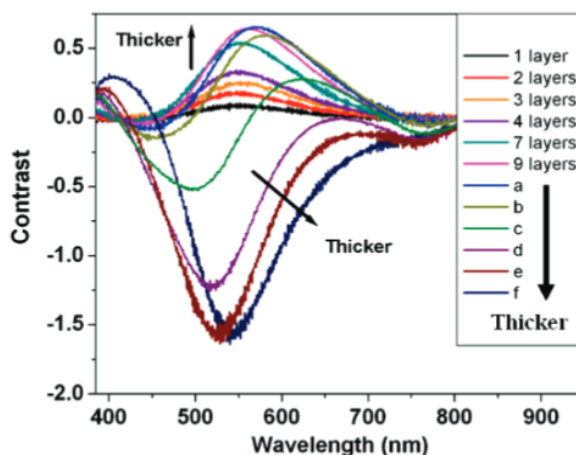
**Figure 2.12:** The contrast spectra of graphene sheets from 1-9 layers and a-f for a number of layers bigger than 10 [15].

normal light microscope is made possible once graphene is placed on a 300 nm $SiO_2$/Si-substrate. Fig. [15] showing the contrast spectra for different numbers of graphene sheets (from one to nine layers), as-well-as samples a-f showing samples thicker than ten layers. This helped us clarify, that in order to see all the layers, the most ideal wavelength for our light-source would be at 550 nm, allowing us to see all sheets with naked eye. This would be sufficient for our use of the microscope, as we mainly needed it for the flake search. In later experiments the thickness will not always be mentioned, since the same 300 nm-$SiO_2$/Si substrate is used.

## 2.4 Atomic Force Microscope

Atomic force microscopy (AFM) belongs to the category of scanning probe microscopy (SPM) known for its exceptional high resolution, typically operating at the atomic scale. In this microscopy technique a fine-tipped probe (typically with a size of few nanometers) scans across a surface while monitoring the interaction between the probe and the sample. By bringing the tip very close to the material, we achieve interactions at an atomic level, which we are able to analyze in order to extract different profiles (in our case the interest lies in the height profile).
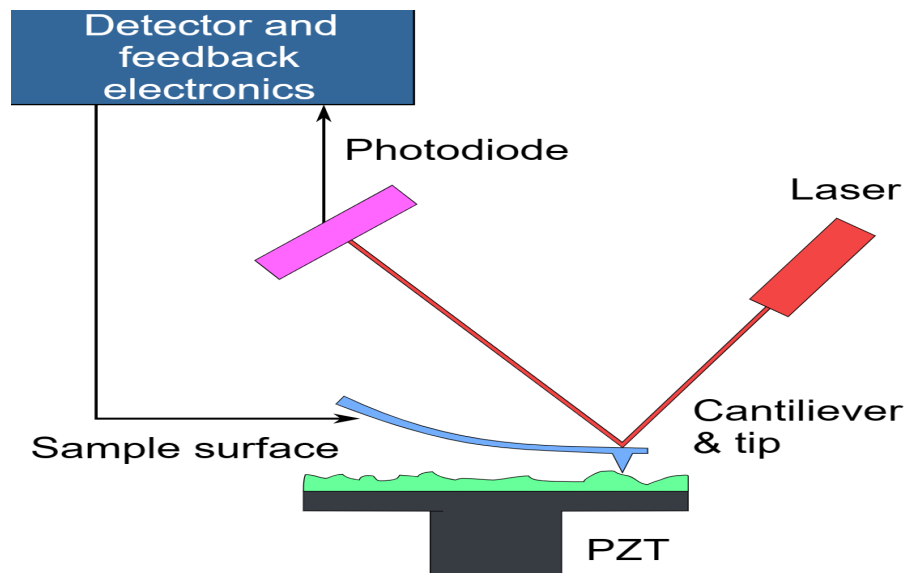
**Figure 2.13:** An AC voltage causes the cantilever to vibrate at or near its resonant frequency. The output of the circuit is an AC voltage proportional to the oscillatory amplitude of the cantilever. The circuit produces an alternating current (AC) voltage that correlates with the oscillatory amplitude of the cantilever. This resulting output is directed to the AFM controller via the signal access module. The x-y-z scanning in the microscope is facilitated by utilizing the piezotube. [16]

The scanner in an Atomic Force Microscope (AFM) functions as a piezoelectric micro-cantilever. Its oscillations over the material generate a topographic image of the surface. To ensure the integrity of both the AFM and the probe, a feedback loop is employed to control the distance between the tip and the probe. The piezoelectric nature of the scanner is crucial for sensing interactions with the material. When a voltage is applied, the piezoelectric scanner bends, expands, and contracts predictably. For precise tracking of surface topography, a photodiode detector monitors changes in the contact between the tip and the probe. If contact alters, the cantilever bends or deflects, a signal detected by the photodiode. This information is then fed back to the computer, facilitating adjustments in the tip's height to adapt to the material. Simultaneously, a surface topography map is generated. This iterative process involves a continuous comparison between the detector

signal and the setpoint, ensuring accurate and dynamic imaging.

## 2.4.1   AFM Modes [1]:

Contact Mode: The tip is perpetually in contact with the sample. The tip is attached to the end of a cantilever with a low spring constant. When the scanner gently traces the tip across the sample, the contact force causes the cantilever to bend in order to capture the changes in topography. The force on the spring is calculated by Hooke's Law $F = -k \cdot x$ , where $F$ is the Force, $k$ is the spring constant and $x$ is the cantilevers deflection.

Non-contact Mode: Non-contact AFM is one of the vibrating cantilever techniques, where a stiff AFM cantilever is vibrated near the surface of the sample. The cantilever vibrates near its resonance frequency and once the system detects a change in the resonance frequency or the amplitude of the cantilever, and manages to adapt through the z-feedback in order to never contact the surface the surface with an oscillating probe tip. As the z-feedback is minimized, the amplitude changes are constantly changing with a change in surface and therefore it is easy to manage topography imaging.

Tapping Mode: This is the most commonly used method for an AFM use. It consists in imaging the topography by lightly tapping the surface. It is a great mode, also allowing us to also scan wider areas, where the sample may have big changes in the surface. This last method is the one also used by us on the AFM Dimension Icon from Bruker in order to scan the flake before and after cutting to know how the flake is assembled.

## 2.4.2   Other SPM - Anodic Oxidation

For scanning probe litography (SPL), Local Anodic Oxidation (LAO) has been one of the most robust and versatile SPM methods used, since it got discovered in 1990 [17] and then further improved in 1993 also making it applicable on an AFM [18]. In general, LAO relies on electrochemical reaction driven by a DC voltage, applied between the tip (cathode) and the sample (anode). On the tip apex, once a voltage is applied, there forms a strong localized electric field ( $10^7$ V/m) with two main functions:

- attract $H_2O$ molecules from air and create a nanometer-sized water bridge, connecting the tip's and sample surface,

- the string electric field helps generate ions (e.g. $H^+, OH^-$ and $O^{2-}$, by decomposing water molecules and drive the oxygen-containing radicals (e.g. $OH^-$ and $O^{2-}$ to the samples surface in order to achieve oxidation.

In our case, we are interested in electrode-free LAO (EFLAO) for nanolitography. This means, that the oxidation process works without microelectrode connection and therefore only an AC voltage is applied between the coated tip (e.g. gold) and the $SiO_2/Si$-substrate. After its application, a water meniscus is created, whenever the amplitude of the voltage pulse is above a certain threshold voltage.

The formation of a liquid meniscus initiates an oxidation reaction when an applied voltage pulse disrupts the covalent bonds within the water molecules. The liquid bridge provides the ions (OH, O) needed to form the oxide and confines the lateral extension of the region to be oxidized. The higher the relative humidity, the larger and longer the meniscus will be, allowing to etch more material at once with the disadvantage of being less precise.
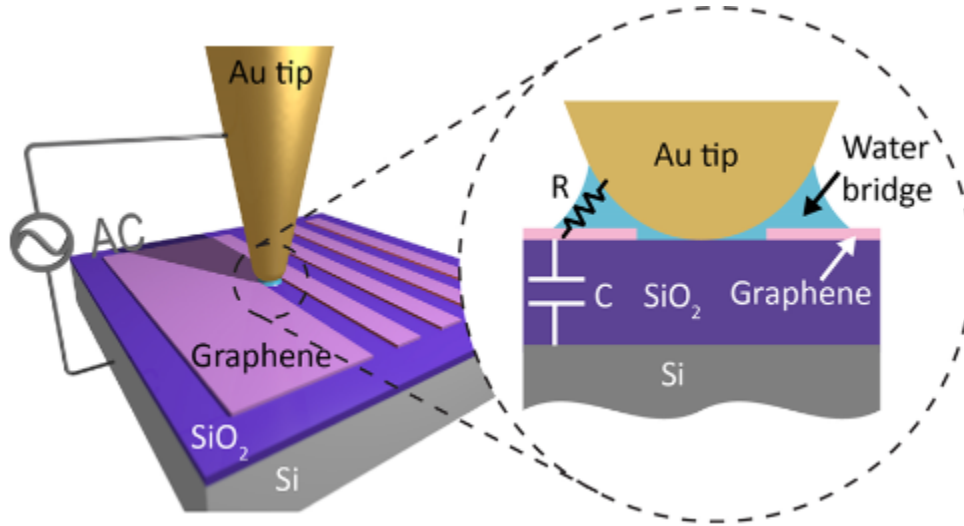


**Figure 2.14:** Illustration of EFLAO. Scheme, in which the electrochemical reaction (possible through the water meniscus) is driven by an AC-voltage applied through the $SiO_2$/Si substrate without any electrode directly connected to the sample. Front-view zoom-in of the area, where the chemical reaction takes place through the water meniscus.
January 26, 2024, Nano. Lett. 2018, 18, 8011-8015 [19]

In comparison to the DC-LAO, which usually very easily creates oxide residues, one can achieve a much higher resolution and etching quality through the AC-voltage. As we know that the water meniscus plays a key role in the etching process, the relative humidity level plays an important role during the process.

The chemical reactions that rule the process of local anodic oxidation in graphene are:

$$C + H_2O \longrightarrow CO + H_2 \qquad (2.23) \qquad C + 2\,H_2O \longrightarrow CO_2 + 2\,H_2 \qquad (2.24)$$
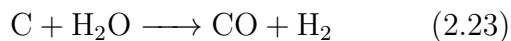
The structure of the exfoliated substrate can be looked at as a capacitator with impedance $\frac{1}{j\cdot 2\cdot \pi \cdot f\cdot C}$, where $j$ is an imaginary unit, $C$ is a capacitance and $f$ the frequency. The formed water bridge can be seen upon as a resistor R, hence being in sequence with the impedance of the graphene-$SiO_2$/Si, it can be looked at as a series of resistance. Like this, one can calculate the voltage drop $U_R$ across the water bridge, from the AFM tip to the sample:

$$U_R = \frac{U \cdot R}{R + \frac{1}{\omega}} \qquad (2.25)$$

# Chapter 3

# Methods

## 3.1 Sample Preparation

This section will provide a step-by-step guide on how samples are prepared in the cleanroom, intending to use them for processes such as graphene cutting, stacking, and more. Precision in each step is crucial to avoid errors later in the process, which could lead to wasted time and resources. Every procedure will be thoroughly discussed, elucidating the purpose behind each step and the methods employed to attain specific results.

### Pre-Exfoliation

Before initiating the exfoliation process, preparation of the substrate, where the flakes will be located, is essential. This preparation involves selecting the appropriate substrate with the corresponding thickness (Ch. 3.1.2), cutting it to the correct chip size, and thoroughly cleaning it. The objective is to facilitate easy adhesion for the graphene flakes. To achieve the desired chip size, we use a diamond tip to scratch the wafer's edge, separating the required amount from the rest of the wafer. However, this process generates a considerable amount of



**Figure 3.1:** From left to right: Pressurized $N_2$ gun, Acetone and Isopropanol, cleaned silicon chips

residue, which could adversely impact the purity of our flakes. To address this, we undertake a cleaning process for the chips. Initially, we use compressed air to blow off larger dust particles. Subsequently, we immerse the chips in a bath of acetone and isopropanol to eliminate finer and more adherent dirt. Finally, we dry the chips with compressed air. These four simple steps aim to provide an initial quick clean-up of the chips, ensuring they are free from dirt and won't contaminate subsequent flake deposition.

In the event that an even cleaner flake is required to enhance the adhesion of graphene from the tape to the chips, plasma etching can be employed. This process effectively cleans the chips of any organic material without adversely affecting the substrate for subsequent processes like lift-off. The underlying principle involves the production of plasma through

the dissipation of electrical power onto the medium, in this case, Silicon. In this process, electrons in the gas, carrying the majority of the power, initiate collisions with atoms and molecules situated on top of the substrate [20].

To execute this, we conducted plasma etching at low pressure (0.5 mBar) for 3-5 minutes. This duration allows the electrons to interact primarily with the upper part of the substrate, preventing excessive damage to the $SiO_2$-layer where the later exfoliation is to take place.



**Figure 3.2:** Giga-Etch 100-E Plasma Etcher while doing $O_2$ Plasma at 285W, 0.5mBar for 3 minutes
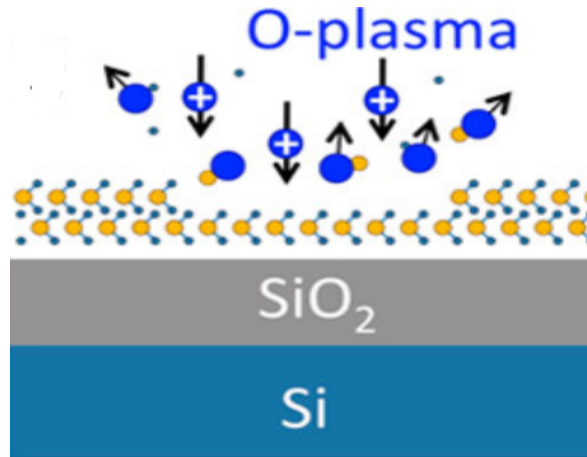


**Figure 3.3:** Representation of electrons from $O_2$-gas interacting with atoms/molecules located above $Si/Sio_2$-substrate. Adapted from Fig.5 of [21].

There have been various approaches regarding the choice of gas for plasma etching materials. In our case, we exclusively utilized oxygen due to its six valence electrons, which potentially facilitate easier interaction with organic materials compared to argon, a noble gas that is less likely to release electrons. Additionally, etching with argon is a purely mechanical process, while etching through oxygen plasma involves a chemical component. With the majority of the power carried by the electrons in the gas, collisions are initiated with atoms and molecules on the substrate's surface, leading to a more thorough clearing of the $SiO_2$. Once the cleaning is executed accurately, we proceed to the mechanical exfoliation stage.

### 3.1.1 Mechanical Exfoliation of Graphene

To fabricate mono- to few-layer graphene and other 2D materials, various methods have been developed over time. These methods can be categorized into dry and wet exfoliation processes, including fluid dynamics, sonication, ball milling, detonation, and, finally, mechanical exfoliation [22]. In our case, we employ the mechanical exfoliation process, which was first utilized in 2004 for the exfoliation of graphene and other 2D materials [23]. This method allows for the production of high-quality, large-area graphene flakes starting from a bulk material like graphite. The following section provides a step-by-step representation and explanation of how mechanical exfoliation is carried out.
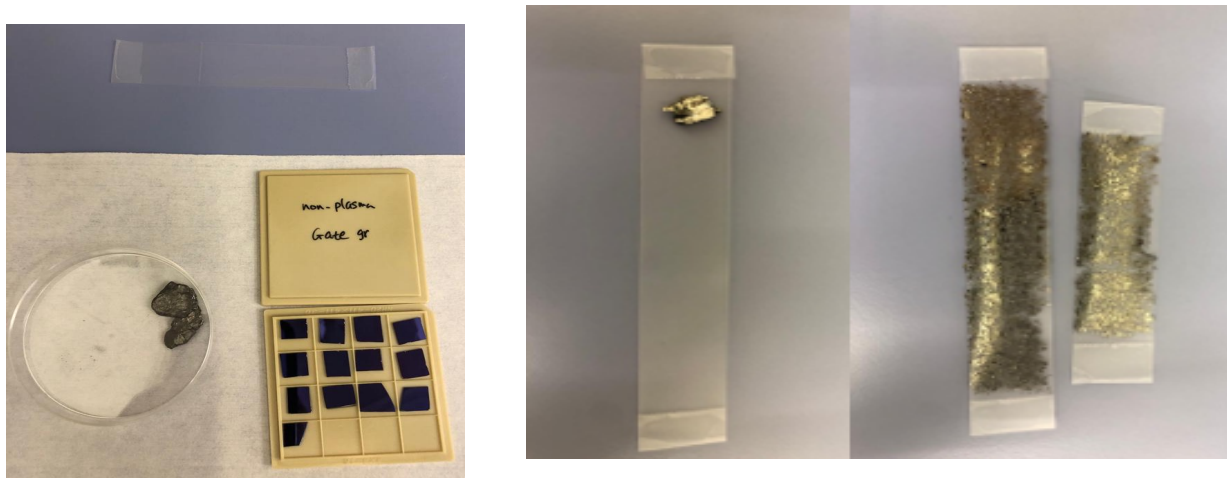


**Figure 3.4:** <u>Left:</u> Materials needed for mechanical exfoliation.
<u>Right-Left</u> Piece of tape with bulk material at one extremity.
<u>Right-Right:</u> Tape filled after multiple strip-offs in order to layer down the bulk material took place, in order to create multiple graphene layers.

For this process, a 300 nm thick $SiO_2$ layer on a Si substrate and regular adhesive tape serve as the transfer medium. The procedure involves slowly placing the bulk material on one end of the tape and gently pressing it down. Subsequently, the bulk material is lifted off, leaving a specific number of layers adhered to the tape. This step is repeated 2-3 times to densely fill one outer edge of the tape stripe. To fill the remaining portions of the Scotch tape, empty tape sections with fresh glue are used, pressed onto the previously filled edges. Stripping off the tapes allows for the separation of multiple stacked graphene layers [21]. The force applied to the material through the Scotch tape is stronger than the Van-der-Waals forces between the graphene layers. If the filled tape is dense but has excessively thick layers, noticeable by a very dark and shiny appearance, a daughter tape can be created by attaching a new piece of Scotch tape onto the previously filled one (Fig. 3.4).

Through multiple attempts, it became evident that not every exfoliation process resulted in high-quality, large-area graphene flakes. The primary cause for this variation lies in the different types of forces applied to the bulk material during the peeling off of the Scotch tape. The ideal scenario involves only normal forces, as these directly separate the layers. In cases where shear forces or fragmentation occur, the graphene layers are still separated, but the drawback is the potential presence of folds and crumples, compromising the homogeneity of the flake's area.
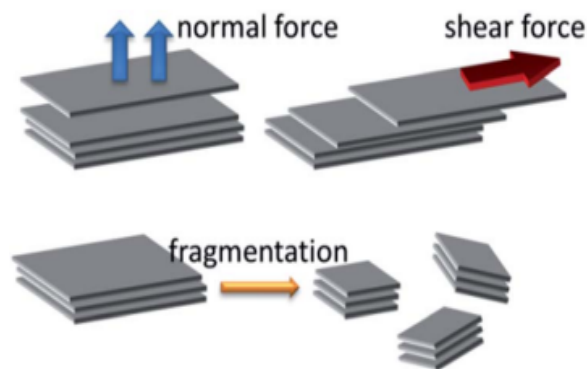


**Figure 3.5:** Model for possible types of forces applied to graphite while mechanical exfoliation is made. Adapted from Fig. 1 of [22].

Once a Scotch tape is completely filled, clean chips are placed onto the tape with the polished side facing upwards. By applying pressure to the back side of the chip, the graphene adheres to the $SiO_2$/Si-chips, and air between the chip and tape is forced out, ensuring a firm attachment (Fig. 3.6). To enhance adhesion further, the tape with the chips is placed on a heating plate at around 110 °C for 4 minutes, facilitating the evaporation of water/moisture (Fig. 3.7). Finally, chips are gently removed from the tape with tweezers and positioned under the microscope.
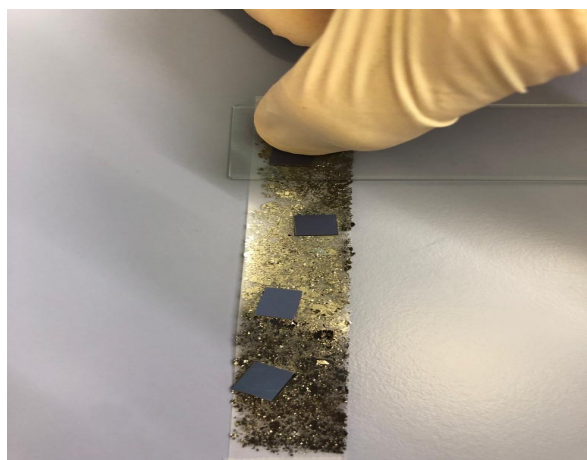


**Figure 3.6:** Application of force through a microscope glass slide, on the backside of chip in order for graphene to stick to $SiO_2$.



**Figure 3.7:** Microscope glass slides pushing keeping scotch tape with 300nm $SiO_2$/Si-substrate on a hot plate

## 3.1.2   Flake Search

Following the completion of the mechanical exfoliation process, an initial step involves identifying potential candidates for subsequent procedures. To pinpoint the location of flakes on the chip later on, we commence by creating a "flake map" (Fig. 3.8). Each chip is scanned, typically at X20 magnification, to locate flakes suitable for cutting and stacking. Our primary focus is on mono-, bi-, and trilayer flakes. Using a camera integrated into the light microscope setup, we project the image onto the computer screen, enabling us to measure its size and intensity differences (Fig. 3.9). This initial approximation helps us precisely determine the number of layers, with each ten steps corresponding to one layer of graphene. Furthermore, an example illustrates the process of flake search:
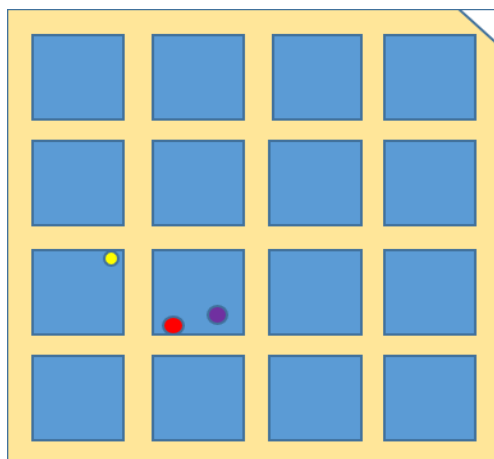
**Figure 3.8:** Model showing 16 chips held in a container, used to mark possible candidates in a PPT Slide through a coloured dot or cross.
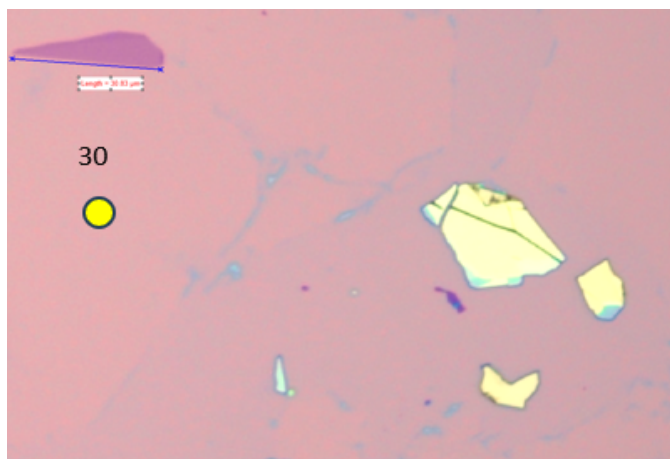
**Figure 3.9:** Example of a flake under the microscope with normal light. Possible candidate marked with yellow dot, measured out lenght and difference in intensity compared to substrate.

After marking all potential flake candidates on the map, the next step involves anodic oxidation with the AFM. Having an approximate understanding of the flake's position, orientation, and thickness provides a valuable advantage in this process.

## 3.2    Anodic Oxidation with an AFM for cutting

The next step is the oxidation of the graphite flakes in order to achieve the cuts. In our case, we use

- AFM: Dimension Icon from Bruker,

- Software: NanoScope, Experiment: Other SPM, Cutting: NanoMan,

- Tips: Arrow-NCPt-50 tips from NANOWORLD.

The tips have following properties:

| Thickness: 4.6 µm Length: 160 µm Width: 45 µm | Resonance Frequency: 285 kHz Force Constant: $42\frac{\text{N}}{\text{m}}$ | Coatings: Tip side: Pt/Ir-coat Detector side: Pt/Ir-coat |
|---|---|---|

**Table 3.1:** Properties of Arrow-NCPt-50 tips from NANOWORLD [24]

The AFM was located in an enclosure hood in order to keep the humidity level stable and not affect the procedures. We started always by inserting the right tip in the holder and then again in the scanner head (Fig. 3.10, (8)).
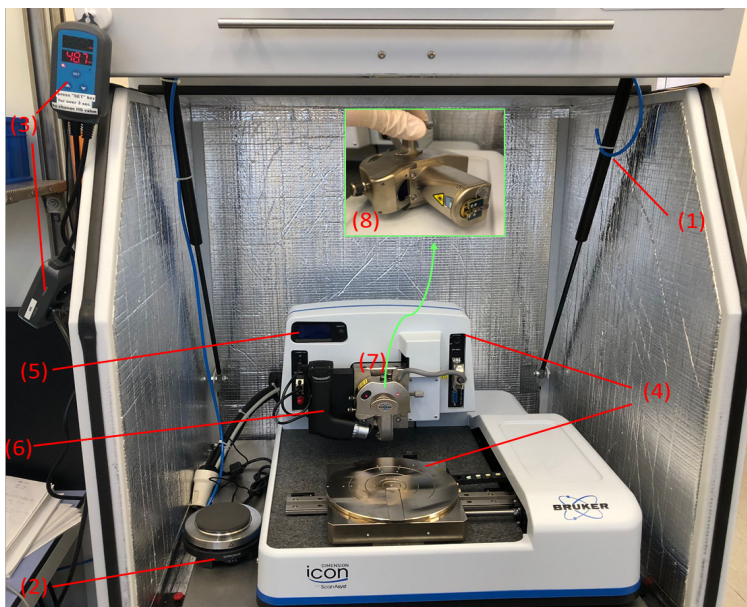


**Figure 3.10:** AFM-Components

1. Nitrogen inflow

2. Heating Plate (levels 1-6)

3. Humidity control

4. Vakuum switch for table

5. Screen

6. Camera

7. Scanner Head (mounted)

8. Scanner Head (front) with tip an holder

Once the scanner head is reinserted into the AFM (Fig. 3.10, (7)), the laser needs to be calibrated. This is achieved by initially moving it with the upper knobs and then with the side knobs. When a good reflection is achieved, the laser should be barely visible on the floor, and a reflection should be visible in the scanner head. On the display (Fig. 3.10, (5)), one should see 0.00 on both horizontal and vertical axes and a maximum on the SUM.

To stabilize the exfoliated 300 nm $SiO_2$/Si-chip, the vacuum is turned on (Fig. 3.10, (4, top)), and the chip is placed above the table's hole (Fig. 3.10, (4, bottom)). The setup is then concluded by auto-tuning the cantilever, determining the drive amplitude and frequency. Subsequently, the table is navigated under the scanner head to locate the desired flake. Considering how the chip should be rotated becomes beneficial to achieve the desired orientation for imaging the flakes.

Before initiating the cutting process, a preliminary image of the flake is obtained by vaguely choosing parameters and starting the scanning process. Image quality is especially dependent on the amplitude setpoint, lines, frequency, and speed of the scanner head. It is crucial that the trace and re-trace signals match, indicating that the AFM captures an identical signal in both scanning directions. The shape and height of the flake should be briefly comparable with the image from the light microscope. Once the AFM has scanned the flake for the given size, we can proceed to the anodic oxidation process.

## 3.2.1 First cuts

It is crucial to have the right tip inserted, preferably made with a conductive coating material to ensure conductivity. To create simple cuts, one manually draws the lines into the NanoMan window using the mouse. The software then displays the scan done beforehand along with the inserted lines for the planned cut. To initiate the cuts, one needs to adjust the following parameters:

**Table 3.2:** Segment

| XY velocity | 1 µm/s |
|---|---|
| Tip voltage | 0 V |

**Table 3.3:** Connect

| Feedback Mode | off |
|---|---|
| Z Distance | 500 nm |
| Z Velocity | 250 nm/s |
| XY Velocity | 1 µm/s |

In this process, the "Segment" window controls the tip movement in contact-mode before and after cutting, while the "Connect" section manages the cutting in tapping mode. Once the parameters for these two windows are set, one can "Enable" the Lock-In2, select "Tip," and insert 150 kHz in the "Drive2-Frequency" and 10,000 mV in the "Drive2-Amplitude". With these settings in place, one can verify the number of elements (single lines) to be cut and initiate the process by selecting "Do it." During cutting, each completed element is marked in green. After cutting, the software allows for the insertion of more cuts in the same area or elsewhere by repeating the same process.

### 3.2.2 Cutting in Patterns - AutoDesk AutoCAD

Utilizing AutoCAD to import vector designs into NanoMan can significantly enhance precision and efficiency compared to single lines and direct drawing, especially when dealing with complex geometries that require precise proportions.

**Cutting Procedure**

AutoCAD is employed when precise proportions and intricate geometries are essential. For instance, designing graphene fingers for contacts may not necessarily require AutoCAD, as it can be more time-consuming, and control over density may be compromised. However, for cases where exact proportions are crucial, AutoCAD proves beneficial. The process of importing designs from AutoCAD into NanoMan is relatively straightforward. Once the design is created using the appropriate tools in AutoCAD (Fig. 3.11), the file can be exported. It is crucial for the design to be unitless during the export process.
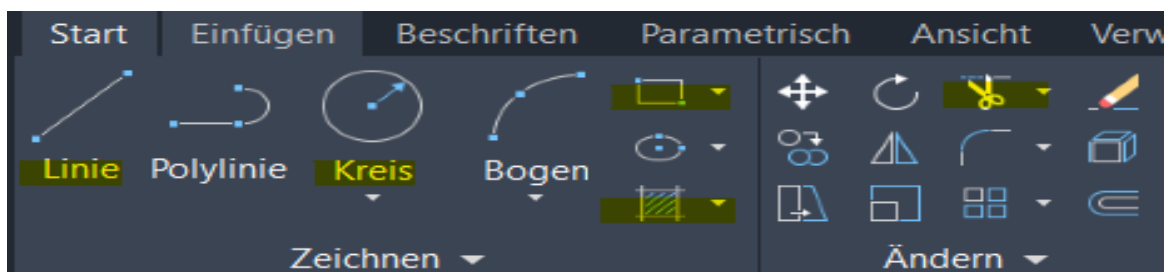


**Figure 3.11:** Possible tools visible in the Start-Menu of AutoDesk AutoCAD Software. Highlighted are the ones which are mandatory in order to create 2-dimensional figures, cut them, hatch them, etc.

To export the drawing from AutoCAD, follow these steps: "Start" → "Export" → "Other Formats" → filename.wmf. This will allow you to obtain the drawing as vectors. In NanoMan, import the drawing through the following steps: "Vector Import" → "Open Vector" → choose the drawing to insert and click "Open." To display the drawing, select "Show Vector on Image." Then, apply changes to the XY position using "X/Y center" and adjust the size through "Height" and "Width." Afterward, click "Make Path," save it ('filename.pth'), and move on to the "Path" window. This process allows you to import the drawn file as vectors.

Now, open the pth-file again in the "Path" window to insert the specified settings (Tab. 3.2, 3.3). Ensure that all parameters, including those of Lock-In2, are correct. Pressing "Do it" in the interface will initiate the cutting process.

In Fig. 3.12, you can observe the three windows where the previously explained values/parameters need to be implemented for cutting. If any parameter is omitted from the "Lock-In2" window or changed incorrectly, the cuts may not work. Similarly, changes to parameters in the "Connect" window might result in imprecise or incomplete cuts.
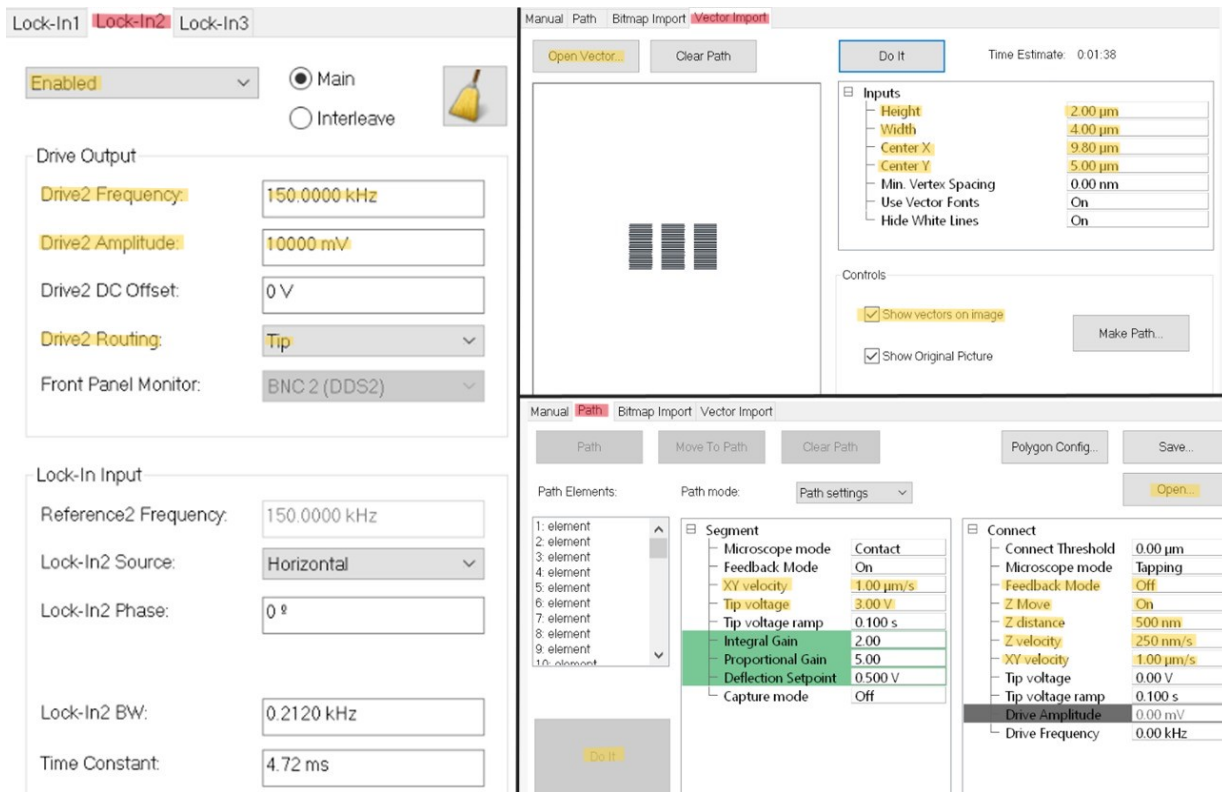
**Figure 3.12:** <u>Left:</u> Lock-In2 interface with values to apply AC-voltage on the tip.
<u>Top right:</u> Import of a .wmf file from AutoCAD and adjusting its position and size.
<u>Bottom right:</u> Parameter window from "Connect" and "Segment" with all values for cutting.

Fig. 3.13 showing a model of a brief walkthrough of an AFM before, during and after etching through anodic oxidation.
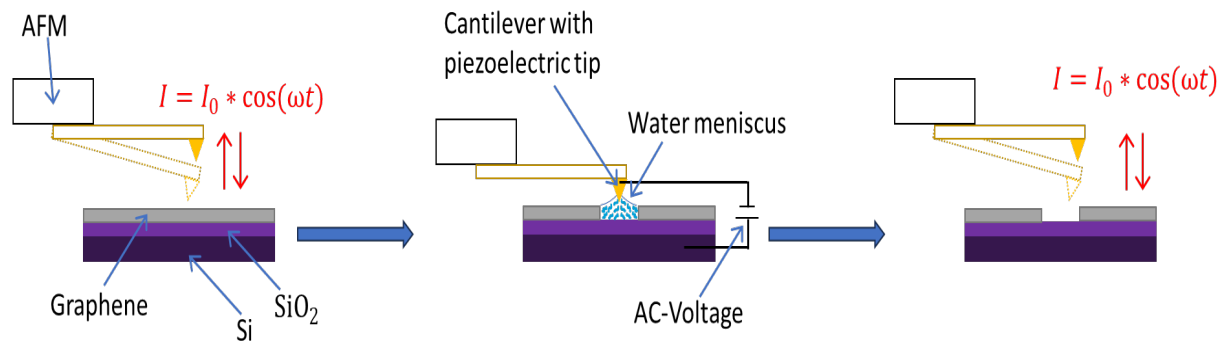


**Figure 3.13:** <u>Model showing:</u> (1) AFM scanning in non-contact mode (2) AC-voltage applied, creating water meniscus for etching (3) AC-voltage removed and scanning like in (1).

## Patterns/Designs

Here are shown the four structures which were implemented from AutoCad into NanoMan. The stripes show the area which is going to be implemented and then cut. Each structure has its own purpose, as with each of them a specific device can be produced through stacking, like briefly explained in the introduction.
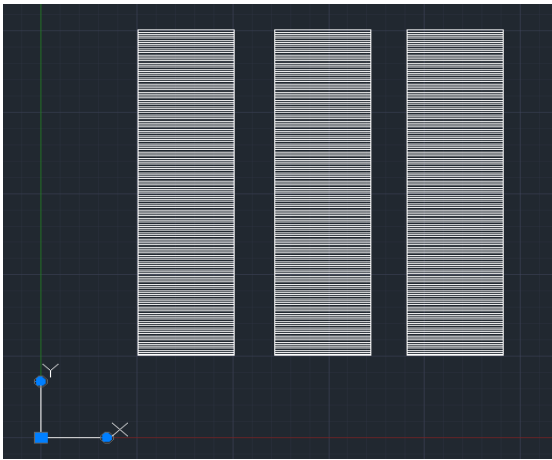


**Figure 3.14:** Fingers for contacts
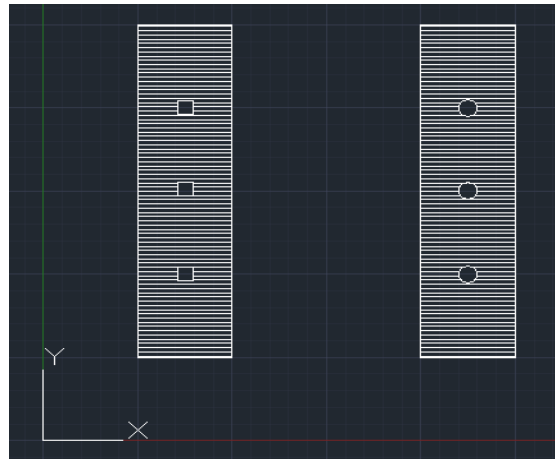


**Figure 3.15:** Dots/Squares for Tunneling
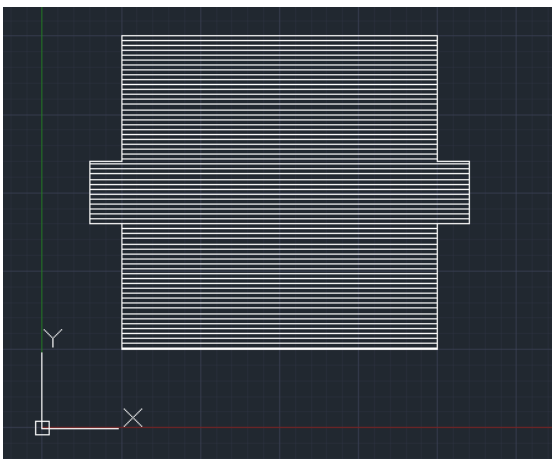


**Figure 3.16:** Ring structure for SQUID
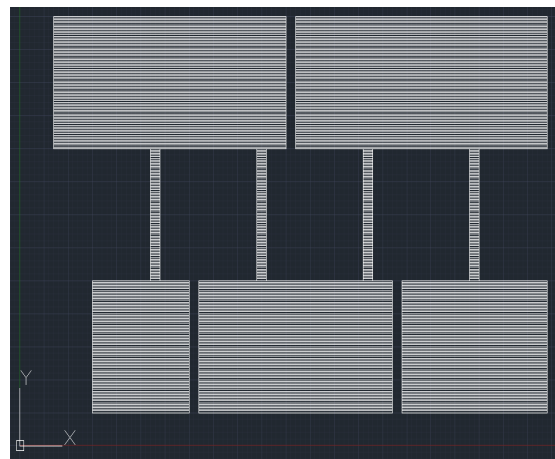


**Figure 3.17:** Contacts with regions

**Design Development for Improved Cuts**
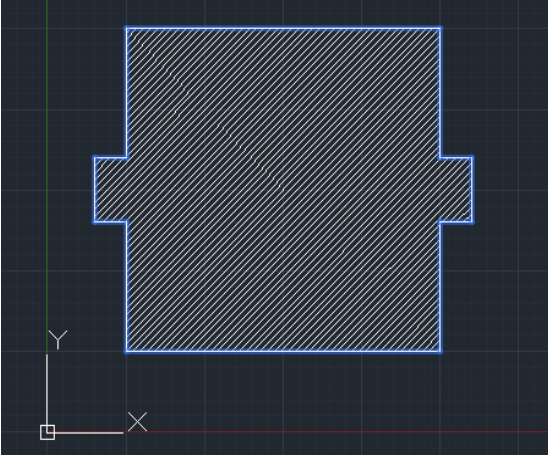


**Figure 3.18:** Hatching: "ANSI31"
(Angle: 0 deg, Scale: 1)
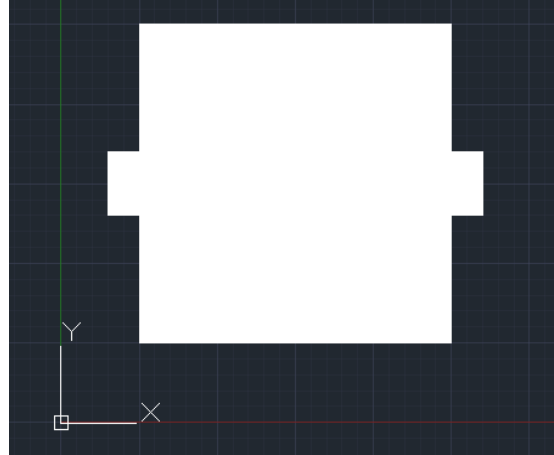


**Figure 3.19:** Hatching: "FULL"
(Angle: 0 deg, Scale: 1)
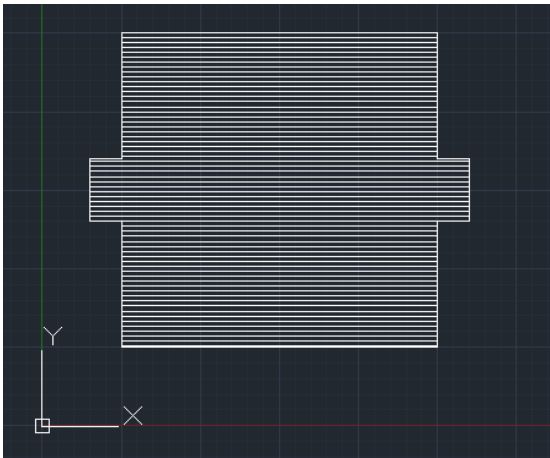


**Figure 3.20:** Hatching: "ANSI31"
(Angle: 315 deg, Scale: 1)
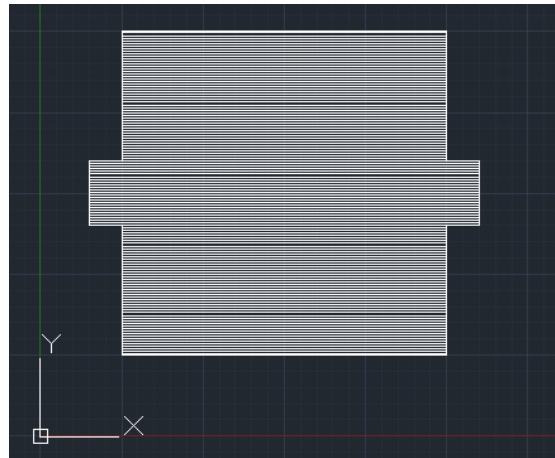


**Figure 3.21:** Hatching: "ANSI31"
(Angle: 315 deg, Scale: 0.5)

The pictures, arranged from left to right and top to bottom, illustrate the evolution of the pattern used for cutting. In the next chapter, I will present the interim results of some cuts, which have enabled us to understand how the drawing in AutoCAD needs to be adapted. It does not necessarily mean that by using the final design shown in Figure 3.21, every cut will be achieved as planned, but we are confident that it brings us closer to the ideal situation. In the next chapter, the progress will be specifically showcased for the ring structure. Subsequently, the other designs will be presented, with the final hatching criteria incorporated for these.

## 3.3 Stamp for Pick-Up

After the exfoliation and AFM procedures, the cut graphene is picked up using a device known as a stamp. This stamp is comprised of a stack of transparent polymers, including Polydimethylsiloxane (PDMS) and Polycarbonate (PC), placed on a glass slide. The stamp is utilized to pick up a flake of hexagonal boron nitride (hBN), followed by the cut graphene.

The procedure involves following the next steps [25]:

1. Preparing a glass slide with above (from bottom to top): Double-sided tape, Scotch tape (with a hole), PC film, PDMS
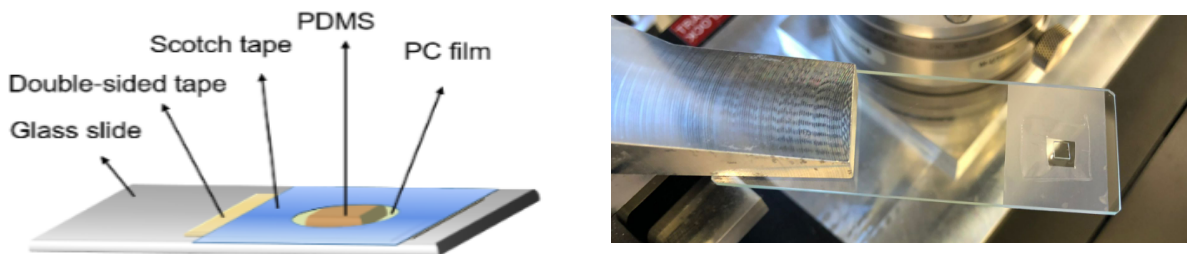


**Figure 3.22:** <u>Left:</u> PDMS/PC stamp for transfering. Adapted from Fig. 3.4: of [25]. <u>Right:</u> Stamp on the microscope ready to pick up hBN. Structure as in the scheme

2. Stamp held by vacuum onto arm. PDMS/PC located onto the bottom side. Approach chip with exfoliated hBN and pick it up

3. After pick up of hBN, since also very sticky, we are able to approach cut graphene/graphite flake and pick it up as well.

4. Drop stack onto clean non-etched 300 nm $SiO_2$/Si substrate.

5. Leave chip with stack in chloroform for 5 minutes.

The results of the pick up process are shown at the end of chapter 4

# Chapter 4

# Results and Discussions

## 4.1 Humidity

As discussed in the fundamentals (Ch. 2), the extent of the etching process is intricately linked to the dimensions of the water meniscus, which, in turn, is influenced by the prevailing relative humidity. To investigate the significance of this dependency, a series of eight incremental cuts was conducted, each differing by 5% in humidity. Commencing at 35% and progressing up to 70%, single side-by-side cuts were performed. Subsequently, the same graphene flake was subjected to tapping-mode scanning. Notably, the results indicate that only three cuts were successfully executed, while one was initiated (45% commenced, 50%, 55%, and 60% were successfully completed) (Fig. 4.1).
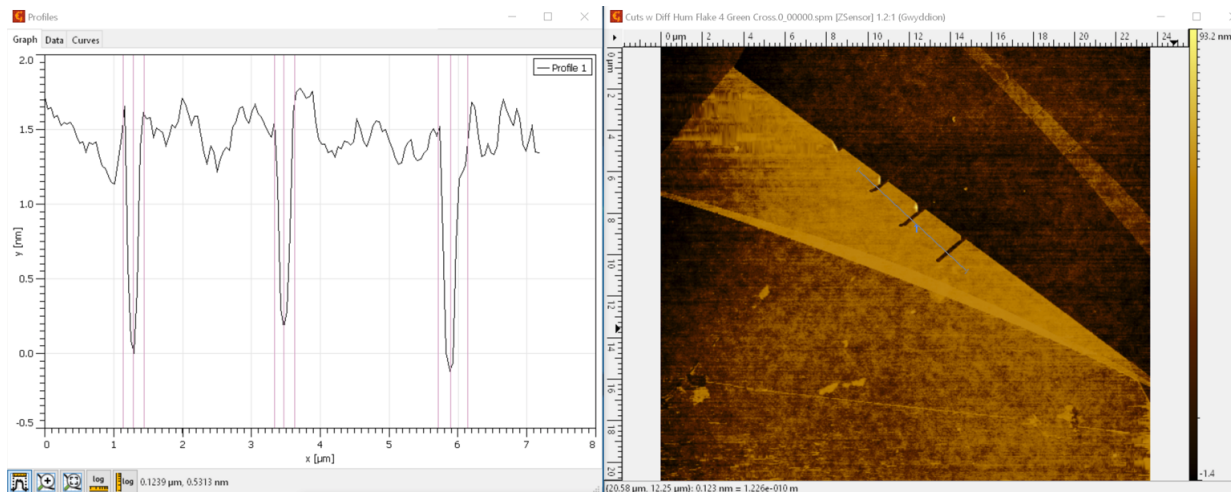


**Figure 4.1:** Flake after process of anodic oxidation was done. Eight cuts with humidity at 35%, 40%, 45%; 50%, 55%, 60%, 65%, 70%; although only four cuts are visible and 3 fully completed. Corresponding to that is an analysis of the depth of the cuts. Both images achieved through "Gwyddion".

During this experimentation, it became evident that the humidity control system exhibited inaccuracies. Upon reaching a reference value, the actual humidity level failed to stabilize long enough for complete oxidation. To enhance control, several strategies were implemented. A key realization was that altering humidity did not necessitate water boiling; instead, the condensation from heating proved sufficient. To achieve this, a smaller 20 ml beaker was utilized and placed on a heating plate set at a maximum setting of '2 out of 6' on the heating scale, preventing water from boiling. This approach ensured that only condensed water coated the container walls, gradually humidifying the AFM glove box at a consistent pace.

Additionally, optimizing the placement of the detector played a crucial role. By positioning it closer to the table with the target, precise measurements were achieved both when increasing humidity with the heating plate and when reducing it through nitrogen inflow from a small tube. These refined methods were consistently applied throughout all the cutting processes, accounting for the varying humidity requirements associated with cutting larger surfaces or achieving precision cuts.

## 4.2   Etched Patterns

In the previous chapter we demonstrated the patterns of interests and how the development of the pattern allowed to achieve results in a satisfactory way. Now are going to be showed results of the cuts. Before being able to cut, all the AFM procedures needed to be done correctly, especially paying attention to flake choice, calibration of the AFM and a good scan with accurate trace&re-trace. Once the cutting design was imported the cuts could be started. I am going to explain the background which caused the design to change into the figured way (Fig. 3.21).

### 4.2.1   Ring Structure

The "ANSI31" pattern is the first one used, since it has multiple single lines. Initially, the relevance of the angle and scale was not known, and therefore the structure of Fig. 3.18 was used.
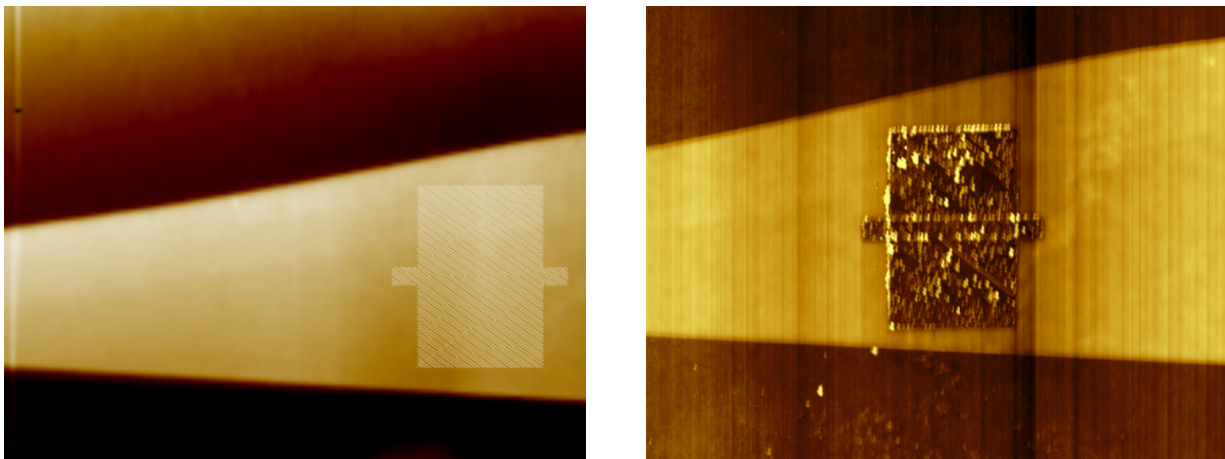


**Figure 4.2:** <u>Left:</u> Image of imported .pth file in NanoMan, showing flake before cutting. <u>Right:</u> Image from Gwiddion of flake after cutting with anodic oxidation of AFM.

It was immediately visible that the structure worked successfully, with the only flaw being the amount of dirt created in the area. This was due to the orientation of the lines not matching the movement direction of the AFM tip. The AFM tip moves parallel to the $x$-axes and therefore, in order to create this design, it needed to engage/disengage for every line/space it encountered. This led to more deposition of oxidized material, since the tip left dirt every time it detached from the surface. Therefore, a solution was needed in order to create less dirt from the oxidation.

Confrontations solicited to try out new hatching stiles. The idea was to make the NanoMan software cut out everything of the interior by drawing a filled pattern in Auto-CAD. This idea was not further researched, since as-soon-as one would import the design of Fig. 3.19 in NanoMan, the filling was taken only as one line and it would not have been possible to cut one area.

Afterwards, the hatching pattern settled back to "ANSI31" like in the beginning. Adapting the angle in order to change the orientation of the lines allowed to match the moving direction of the AFM tip. The direction of the cuts is therefore found to be relevant. For that reason, in case multiple lines are introduced to form a more complex structure, most of them should be matching the moving direction of the AFM tip. The obtained cuts from the design of Fig. 3.20, with pattern "ANSI31" and the new angle to match the tips movement is shown here:
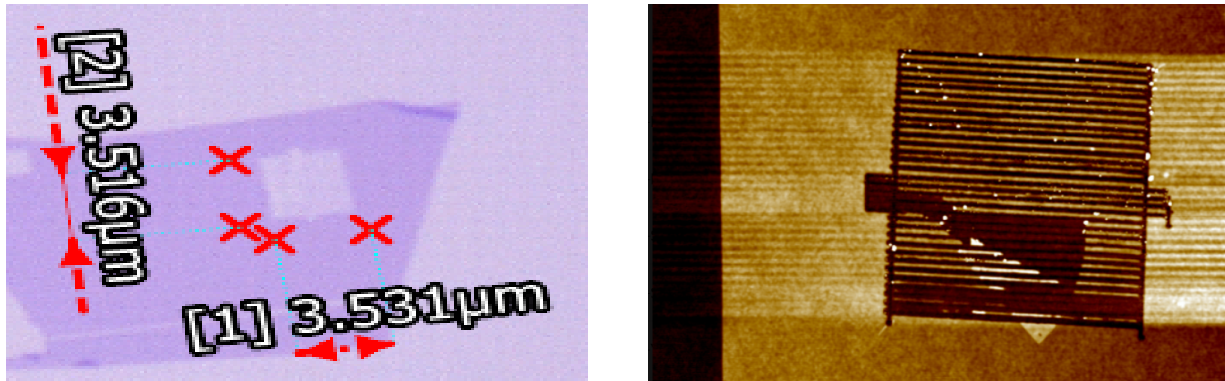


**Figure 4.3:** <u>Left:</u> Image taken with Light Microscope with X100 objective to show outcome of cuts achieved through design from Fig. 3.20. Size $\approx 3.52$ μm $\times 3.53$μm. <u>Right:</u> AFM Tapping mode used to scan flake with more precision, showing rong scaling from hatching.

Fig. 4.3 left was taken to make sure that the outcome was there. It seems like the cut is very precise and therefore, in order to double check, we did another scan under the AFM, zooming in on the cut. From these cuts it is immediately recognisable, that less dirt was formed if the cuts are made in the same orientation of the movement of the tip. It is necessary to add lines by hand, since sometimes the program does not transfer the edges of the design or does not transfer the outline from the AutoCAD design. In doing this, one needs to be very precise in drawing the edges, since a small mistake can lead to poor contouring like on the bottom or right side Fig. 4.3 right. Opposite to the expectations that the left picture gives, the scan made from the AFM shows that the amount of lines was not enough, since multiple sticks instead of a complete area was etched.

Lastly, the biggest change necessary to make was to fix the amount of lines done from the hatching. To do this the scaling of the hatching was changed to 0.5 to double the lines. Hereby, it is important to point out that dependently on the size of the shape a lower/higher amount of lines is needed, requiring a re-calibration for each design change.
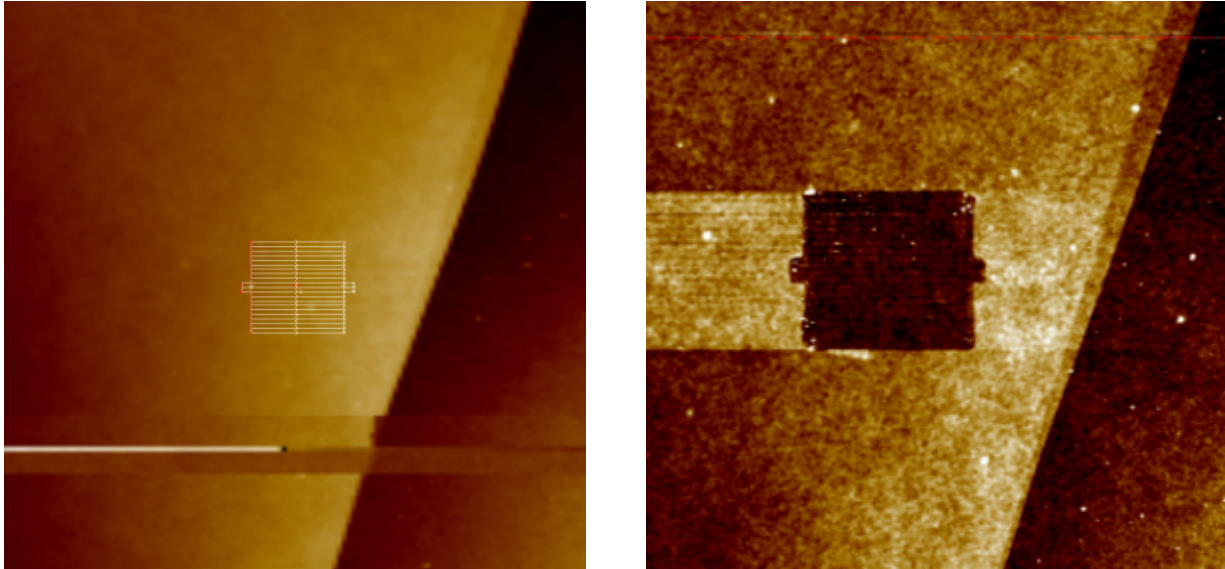


**Figure 4.4:** <u>Left:</u> Scan from AFM of flake with wanted pattern shown in Fig. 3.21 with ratio $1 \times 1$ μm for the square and $0.1 \times 0.1$ μm for the "arms" .
<u>Right:</u> Scan from AFM Tapping mode showing obtained cut.

The outcome, on Fig. 4.4 right, shows only very few white dots, demonstrating that the points which were adapted over time make a difference in the result. Later on, for the explanation and result demonstration of the Pick-Up, we used this outcome. It will get clear, that it is more convenient to achieve cuts which produce less dirt in order to later achieve a precise result. For the pick up this was one of the cuts used.

## 4.2.2   Further structures

For the other patterns/designs the same properties as in Fig. 3.21 were used for the hatching (Type: "ANSI31", Angle: 315°, Scaling: 0.5). I will show these here and explain eventual problems encountered during the anodic oxidation.

**Dots/Squares Structure**

Initially, the idea was to design a square with the inside of it cut out except for small dots (see right side of Fig. 3.15). The issue was how the design from AutoCAD was transformed into NanoMan when importing it. Since the dots were very small, and the NanoMan only knows straight lines and not curves, the round structure was formed by multiple small lines in different directions. This forces the tip to engage and disengage multiple times and creates loads of dirt, leading to a more squared than circular shape. Sequent to the left
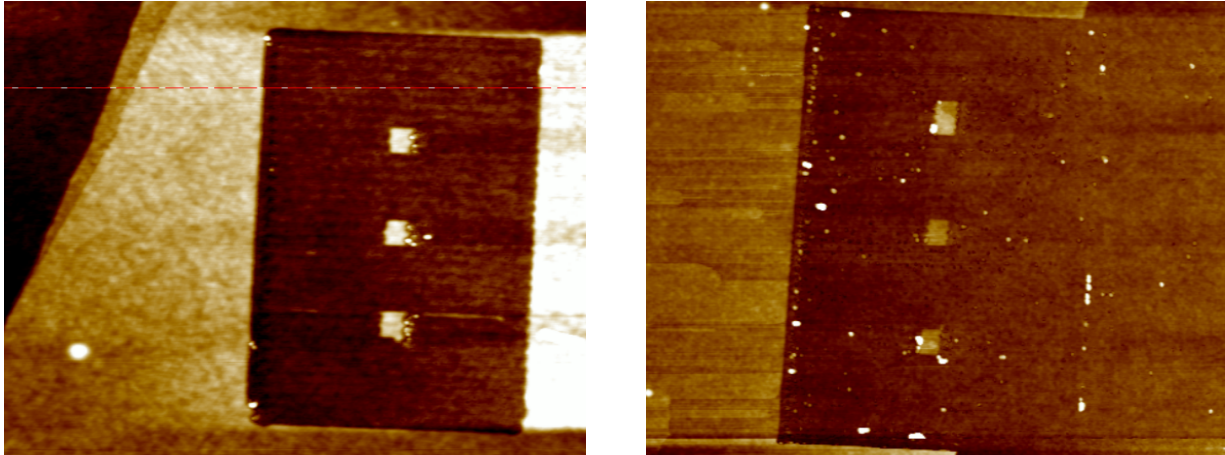


**Figure 4.5:** <u>Left:</u> Scan after anodic oxidation with right pattern of Fig. 3.15.
<u>Right:</u> Scan after anodic oxidation with left pattern of Fig. 3.15.

image, one can see that too much dirt was deposited on the inside and so not only were the dots replaced by squares, but also the direction of the cut was from the inside to the outside so that the tip would disengage further away from the square, hence leaving less dirt. By doing this one could diminish the size of the squares, whereas it was possible to reach a size of about $200 \times 200$ nm.

The designs shown in Fig. 3.14 and Fig. 3.17 were also included in the process of anodic oxidation through AFM, whereas the results were not satisfactory and therefore are presented in the appendix (Ch. 6).

## 4.3   Pick Up

The process of picking up was done with the help of Ph.D. student Jiazhuo Li, as in order to have a clean stack of 2D materials, precision and experience is needed.

Initially the process was tried with only the stamp, without picking up hBN in between, but to show that the dirt remains on the substrate also pick up through hBN was fine. In order to have a comparison, the process was made once with the ring structure (Fig. 3.16) and once with the squares (Fig. 3.15). The matching corners were signed with a small circle in order to indicate which position the cut got lifted up.

**Ring-Structure**
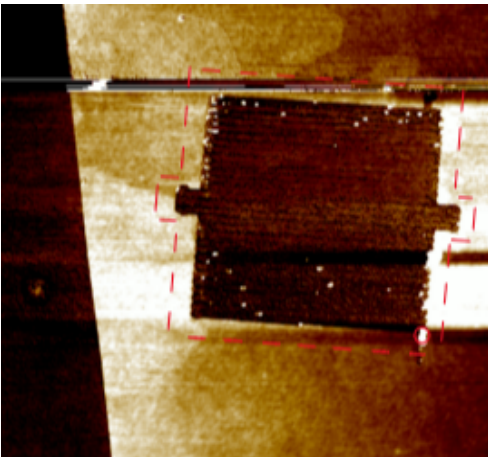


**Figure 4.6:** AFM scan after cutting with pattern of Fig. 3.16
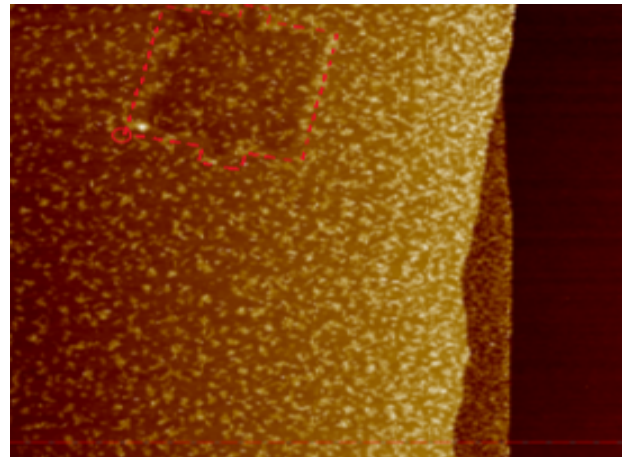


**Figure 4.7:** AFM scan after drop on clean SiO$_2$/Si. hBN is on top, graphite on bottom.

As visible in red, the square got rotated 90 deg towards the left. On the right side of Fig. 4.7, one can see (from right to left), the 300nm SiO$_2$/Si-substrate, cut graphite flake and lastly on top hBN. The dirt which was created through the oxidation from the AFM was not picked up, apart from one small dirt point near the red circle. The small residues distributed all over the place come from the polymers, since they are heated in order to detach from the chip and only pick up the flake chosen. If these do not immediately dissolve well in the chloroform, then it is very difficult to get them away from the substrate. In general the pick up of this structure has worked well, since the shape is not too elaborate and it was transferred so to keep its shape.

**Dots/Squares-Structure**
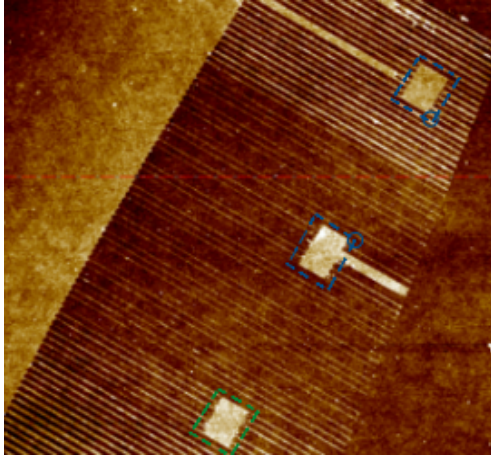


**Figure 4.8:** AFM scan after cutting with pattern of Fig. 3.15
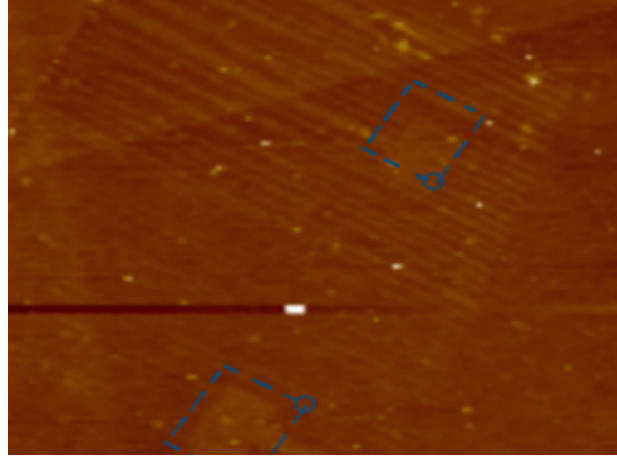


**Figure 4.9:** AFM scan after drop on clean $SiO_2$/Si. hBN is on top, graphite on bottom.

Immediately one recognizes discrepancies between the wanted design of Fig. 3.15 and the achieved cuts of Fig. 4.8. The squares created are very precise but the problem is, that the AFM etched with such a high precision, that also small lines of graphite in between each line got created. Therefore, this result is more a mixture of leaving squares together with lines/bars of graphite. Regardless, pick up of this structure was still executed. Two out of the three squares (in blue) were picked up, as well as the lines. This showed, that also very brittle structures could be picked up. Regarding dirt, the one present on the squares, also stayed on the silicon chip, although there are some bits which got lifted. In this stack the polymers did not leave as much dirt as before, visible from the more mono-coloured picture.

# Chapter 5

# Conclusion

In addressing the primary research of this study - anodic oxidation nanolithography - our investigation delved on pattern creation on multi-layer graphene. Through rigorous analysis we managed to unveil the importance of the humidity, the hatching properties and finally demonstrate successful lift-off of the etched graphene from the substrate through dry transfer with a so-called stamp.

## 5.0.1 Humidity

Recognizing the dependency of the etching process outcome on humidity and the significant influence of the water meniscus formed between the Atomic Force Microscope (AFM) tip and the sample, crucial modifications were implemented to enhance humidity control. This led to the refinement of the AFM box configuration, with the heating plate strategically positioned to induce only water condensation, ensuring a gradual increase in humidity. In the event of surpassing the desired relative humidity, a nitrogen valve, with a modified pressure of 0.3 bar, can be opened to offset the excess moisture. Moreover, for precise monitoring of relative humidity during the etching process, the detector was repositioned closer to the sample, as the humidity near the chip is of particular interest for optimal results.

## 5.0.2 Pattern/Designs

Understanding the correct hatching properties is crucial for optimizing the etching process. A significant finding underscores the importance of aligning the cuts with the tip's movement direction to minimize engagement/disengagement cycles. This ensures continuous etching along a specific line, effectively carrying oxidation material outside the desired structure and preventing deposition in unwanted areas. Adjusting the scaling to vary the number of lines during filling is also crucial. Insufficient scaling may result in only a precise line being etched, leaving small graphene lines between etched parts. The complexity of the structure being investigated further influences etching efficiency.

## 5.0.3 Tip Condition

It is imperative to recognize that the precision of the cuts can be significantly influenced by the condition of the AFM tip. The age and wear of the tip play a crucial role in determining its efficacy during the etching process. For larger surfaces with few intricate features, employing a new tip may present unexpected challenges, since the sharpness of a new tip can lead to a precised etching although the amount of lines in the design is sufficient.

## 5.1   Improvements and Future Works

Given the challenges in achieving complex structures with AFM, one approach for Fig. 3.17 can be to complete the outline first and then fill in the inside in subsequent cycles. Alternatively, the structure can be created by completing squares and bars individually and connecting them later.

For pick-up, experimenting with PDMS/PC alone could improve imaging of etched graphene. This method allows direct AFM imaging on the stamp after cleaning with chloroform, without having the layer of hBN in between.

As mentioned in Chapter 1, these shapes can be used in device construction, making it worthwhile to explore potential outcomes in the future. Junction-based superconducting devices, such as Josephson junctions and SQUIDs, have been introduced recently and enable the exploration of superconductivity and moiré electrons in MATBG. An example is shown in Fig. 5.1, were metallic graphite layers are coupled to the MATBG, through the hexagonal boron nitride (hBN) layers of $\approx 10$ nm thickness. The carrier density in the MATBG sheet $n$ is electrostatically tuned from the capacitance and voltage of both top and bottom gate [26]. Via anodic oxidation one can develop patterns in order to create the shape figured in Fig. 5.1 and etch MATBG, graphite or hBN.
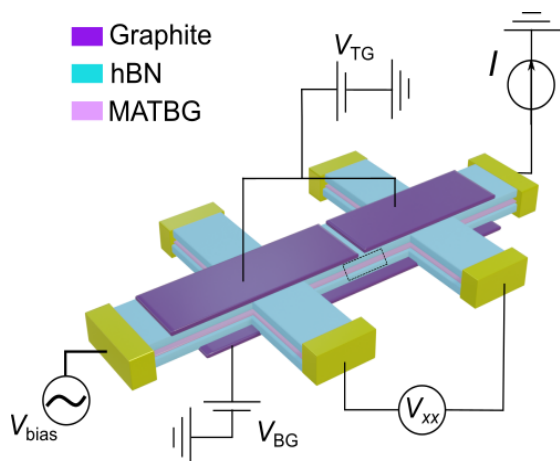


**Figure 5.1:** Schematic of the device and measuring circuit, constructed with graphite, hexagonal boron nitride and MATBG. Adapted from Fig. 1 of [26]
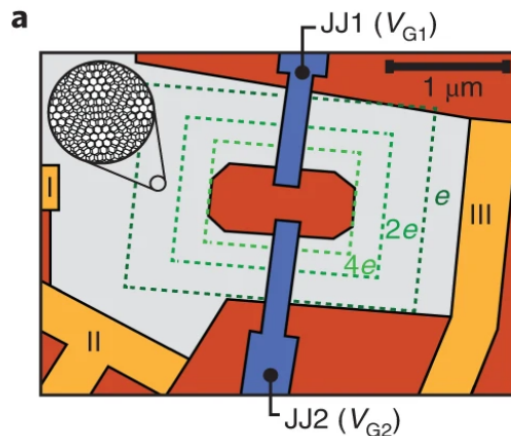


**Figure 5.2:** Schematic of tunable superconducting quantum interference device. Contacts are in yellow, top gates in blue, etched areas in red and MATBG in grey. Adapted from Fig. 1 of [27]

Anodic oxidation also allows to implement etching to create SQUIDs. Instead of using a metal to create JJ1 and JJ2 like in Fig. 5.2, to create these one can etch graphite, allowing to achieve a cleaner device [27, 28, 29]. Further option, which also was experimented, is to include the design from Fig. 3.15. By creating small structures like in Fig. 4.8, it gives the option to built a device with the etched graphene sandwiched in the middle. We use a Van-der-Waals structure to perform tunnelling spectroscopy measurements of the proximity effect in superconductor-graphene-superconductor junctions, allowing us to learn about its electronic properties. The finger with the extended contact region leading outside of the device is here in purple, with the issue that for measurements averaging over the whole region is necessary [30].
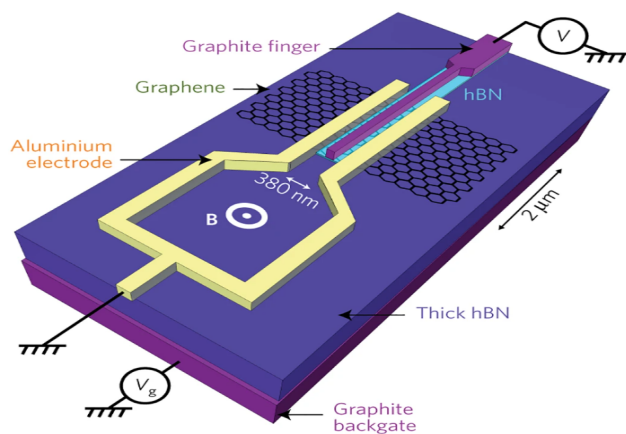


**Figure 5.3:** Device schematic with encapsulated graphene flake and two superconducting electrodes.
Adapted from Fig. 1e of [30]

If the results from the AFM lead to pure dots/squares without fingers attached, then one can improve the tunneling experiment and immediately contact via a metallic extension coming from the top like in this model, hence averaging on a much smaller area [31].
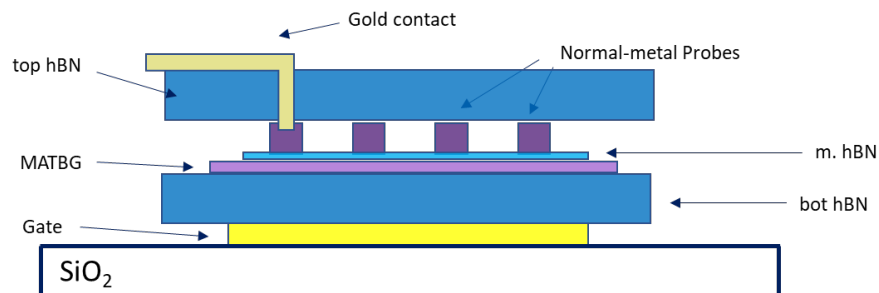


**Figure 5.4:** Scheme showing multiple local graphene top gate with dots/squares contacted from the top by a gold pillar.

# Chapter 6

# Appendix

The motive behind this is that leaving or cutting a 100 nm wide segment is very challenging for the AFM if drawn as a pattern. In the case of the fingers (Figure 3.14), the aim is to oxidize a large part and leave only small bars of graphite (about 2 μm in height and 100 nm width). Both designs were never fully satisfactory in order to produce a stack. Here, one cut from each design made through the AutoCAD designs is illustrated.
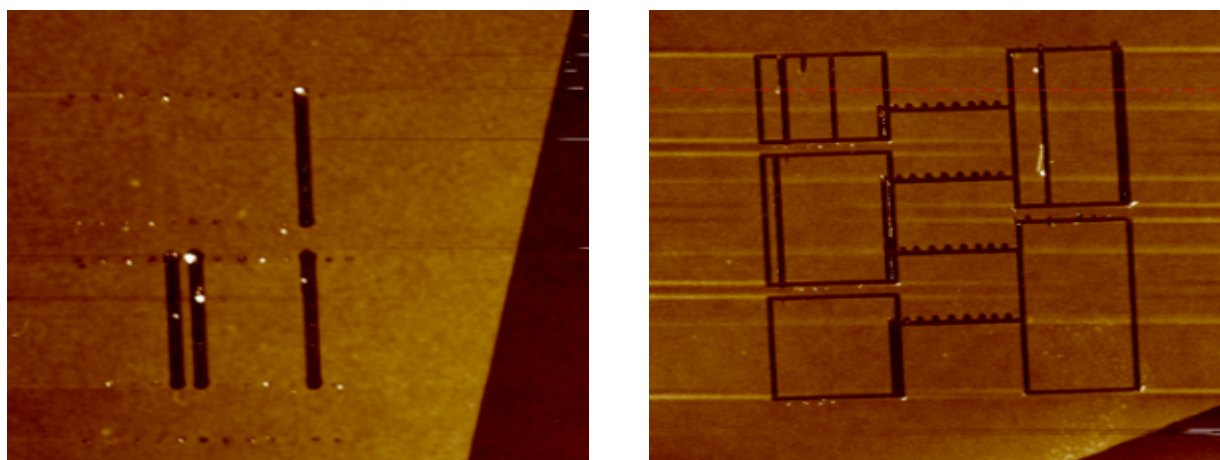


**Figure 6.1:** <u>Left:</u> Scan after anodic oxidation with pattern of figure 3.14. The small dots show where the tip engaged/disengaged. Only four cuts got achieved.
<u>Right:</u> Scan after anodic oxidation with pattern of figure 3.17. Without high precision, only the outline was oxidized and few lines of the filling.

Instead of creating cuts that are very compact and together cutting out a rectangle with "fingers" of carbon in between, as the design shows, only a few cuts were created. This was attempted multiple times, and the best result is the one shown.

On the other hand, the right drawing has a very complicated structure since a set of objects needs to be cut. The best result is shown, and here, only the outline was achieved.

Solutions are discussed in Chapter 4.

# List of Figures

# List of Tables

# Bibliography

[1] www.nanophys.kth. Operating modes bruker afm dimension icon.

[2] A. H. Castro Neto, F. Guinea, N. M. R. Peres, K. S. Novoselov, and A. K. Geim. The electronic properties of graphene. *Rev. Mod. Phys.*, 81:109–162, Jan 2009.

[3] N. M. R. Peres, F. Guinea, and A. H. Castro Neto. Electronic properties of disordered two-dimensional carbon. *Phys. Rev. B*, 73:125411, Mar 2006.

[4] A. K. Geim and Novoselov K. S. The rise of graphene. *Nature Materials*, 2007.

[5] R. Gross and A. Marx. *Festkörperphysik*. De Gruyter Oldenburg, 4th edition, 2023.

[6] Wikipedia: Lennard-jones potential.

[7] J. M. B. Lopes dos Santos, N. M. R. Peres, and A. H. Castro Neto. Graphene bilayer with a twist: Electronic structure. *Phys. Rev. Lett.*, 99:256802, Dec 2007.

[8] Z. Y. Rong and P. Kuiper. Electronic effects in scanning tunneling microscopy: Moiré pattern on a graphite surface. *Phys. Rev. B*, 48:17427–17431, Dec 1993.

[9] Y. Cao, V. Fatemi, A. Demir, S. Fang, S. L. Tomarken, J. Y. Luo, J. D. Sanchez-Yamagishi, K. Watanabe, T. Taniguchi, E. Kaxiras, R. C. Ashoori, and P. Jarillo-Herrero. Correlated insulator behaviour at half-filling in magic-angle graphene super-lattices. *Nature*, 556(7699):80–84, March 2018.

[10] B. Hunt, J. D. Sanchez-Yamagishi, A. F. Young, M. Yankowitz, B. J. LeRoy, K. Watanabe, T. Taniguchi, P. Moon, M. Koshino, P. Jarillo-Herrero, and R. C. Ashoori. Massive dirac fermions and hofstadter butterfly in a van der waals heterostructure. *Science*, 340(6139):1427–1430, 2013.

[11] A. Fischer, Z. A. H. Goodwin, A. A. Mostofi, J. Lischner, D. M. Kennes, and L. Klebl. Unconventional superconductivity in magic-angle twisted trilayer graphene. *npj Quantum Materials*, 7(1), January 2022.

[12] A. C. Ferrari, J. C. Meyer, V. Scardaci, C. Casiraghi, M. Lazzeri, F. Mauri, S. Piscanec, D. Jiang, K. S. Novoselov, S. Roth, and A. K. Geim. Raman spectrum of graphene and graphene layers. *Phys. Rev. Lett.*, 97:187401, Oct 2006.

[13] J. Henrie, S. Kellis, S. M. Schultz, and A. Hawkins. Electronic color charts for dielectric films on silicon. *Opt. Express*, 12(7):1464–1469, Apr 2004.

[14] P. Blake, E. W. Hill, A. H. Castro Neto, K. S. Novoselov, D. Jiang, R. Yang, T. J. Booth, and A. K. Geim. Making graphene visible. *Applied Physics Letters*, 91(6):063124, 08 2007.

[15] Z. H. Ni, H. M. Wang, J. Kasim, H. M. Fan, T. Yu, Y. H. Wu, Y. P. Feng, and Z. X. Shen. Graphene thickness determination using reflection and contrast spectroscopy. *Nano Letters*, 7(9):2758–2763, 2007. PMID: 17655269.

[16] Wikipedia: Atomic force microscope.

[17] J. A. Dagata, J. Schneir, H. H. Harary, C. J. Evans, M. T. Postek, and J. Bennett. Modification of hydrogen-passivated silicon by a scanning tunneling microscope operating in air, April 2018.

[18] H. C. Day and D. R. Allee. Selective area oxidation of silicon with a scanning force microscope. *Applied Physics Letters*, 62(21):2691–2693, 05 1993.

[19] H. Li, Z. Ying, B. Lyu, A. Deng, L. Wang, T. Taniguchi, K. Watanabe, and Z. Shi. Electrode-free anodic oxidation nanolithography of low-dimensional materials. *Nano Letters*, 18(12):8011–8015, 2018.

[20] C. Cardinaud, M.-C. Peignon, and P.-Y. Tessier. Plasma etching: principles, mechanisms, application to micro- and nano-technologies. *Applied Surface Science*, 164(1):72–83, 2000. Surface Science in Micro Nanotechnology.

[21] Y. Huang, E. Sutter, N. N. Shi, J. Zheng, T. Yang, D. Englund, H.-J. Gao, and P. Sutter. Reliable exfoliation of large-area high-quality flakes of graphene and other two-dimensional materials. *ACS Nano*, 9(11):10612–10620, 2015. PMID: 26336975.

[22] M. Yi and Z. Shen. A review on mechanical exfoliation for the scalable production of graphene. *J. Mater. Chem. A*, 3:11700–11715, 2015.

[23] K. S. Novoselov, A. K. Geim, S. V. Morozov, D. Jiang, Y. Zhang, S. V. Dubonos, I. V. Grigorieva, and A. A. Firsov. Electric field effect in atomically thin carbon films. *Science*, 306(5696):666–669, 2004.

[24] M. Becker. Arrow-ncpt-50 tips, nanoworld.

[25] I. Das. Investigation of the interaction driven quantum phases in magic angle twisted bilayer graphene. Jan 2023.

[26] J. Díez-Mérida, A. Díez-Carlón, S. Y. Yang, Y.-M. Xie, X.-J. Gao, J. Senior, K. Watanebe, T. Taniguchi, X. Lu, A. P. Higginbotham, K. T. Law, and D. K. Efetov. Symmetry-broken josephson junctions and superconducting diodes in magic-angle twisted bilayer graphene. *Nature Communications*, (2396), 2023.

[27] E. Portolés, S. Iwakiri, G. Zheng, P. Rickhaus, T. Taniguchi, K. Watanabe, T. Ihn, K. Ensslin, and F. K. De Vries. A tunable monolithic squid in twisted bilayer graphene. *Nature Nanotechnology*, 17(11):1159–1164, October 2022.

[28] L. A. Cohen, N. L. Samuelson, T Wang, T. Taniguchi, K. Watanabe, M. P. Zaletel, and A. F. Young. Universal chiral luttinger liquid behavior in a graphene fractional quantum hall point contact. *Science*, 382(6670):542–547, 2023.

[29] S. Iwakiri, A. Mestre-Torà, E. Portolés, M. Visscher, M. Perego, G. Zheng, T. Taniguchi, K. Watanabe, M. Sigrist, M. Ihn, and K. Ensslin. Tunable quantum interferometer for correlated moiré electrons, 2023.

[30] L. Bretheau, J. I.-J. Wang, R. Pisoni, K. Watanabe, T. Taniguchi, and P. Jarillo-Herrero. Tunnelling spectroscopy of andreev states in graphene. *Nature Physics*, 13(8):756–760, May 2017.

[31] Q. Cao, E. J. Telford, A. Benyamini, I. Kennedy, A. Zangiabadi, K. Watanabe, T. Taniguchi, C. R. Dean, and B. M. Hunt. Tunneling spectroscopy of two-dimensional materials based on via contacts. *Nano Letters*, 22(22):8941–8948, 2022. PMID: 36356229.

Hiermit erkläre ich, die vorliegende Arbeit selbständig verfasst zu haben und keine anderen als die in der Arbeit angegebenen Quellen und Hilfsmittel benutzt zu haben.

München, January 26, 2024

Unterschrift: